

1 Self-Supervised Learning Reveals Clinically Relevant 2 Histomorphological Patterns for Therapeutic Strategies in 3 Colon Cancer

4 Bojing Liu^{1,2,+}, Meaghan Polack^{3,+}, Nicolas Coudray^{2, 4, #}, Adalberto Claudio Quiros^{5, #}, Theodore
5 Sakellaropoulos², Augustinus S.L.P. Crobach⁶, J. Han J.M. van Krieken⁷, Ke Yuan^{5,8}, Rob A.E.M. Tollenaar³,
6 Wilma E. Mesker³, and Aristotelis Tsirigos^{2,9,*}

7 ¹*Department of Medical Epidemiology and Biostatistics, Karolinska Institutet, Sweden.*

8 ²*Applied Bioinformatics Laboratories, New York University Grossman School of Medicine, New York, New York, USA.*

9 ³*Department of Surgery, Leiden University Medical Center, Leiden, The Netherlands.*

10 ⁴*Department of Cell Biology, New York University Grossman School of Medicine, New York, New York, USA.*

11 ⁵*Department of Computing Science, University of Glasgow, Glasgow, United Kingdom.*

12 ⁶*Department of Pathology, Leiden University Medical Center, Leiden, The Netherlands.*

13 ⁷*Department of Pathology, Radboud University Medical Center, Nijmegen, The Netherlands.*

14 ⁸*School of Cancer Sciences, University of Glasgow, Glasgow, Scotland, UK.*

15 ⁹*Department of Pathology, New York University Grossman School of Medicine, New York, New York, USA.*

16 ^{+,#}*authors with equal contribution*

17 ^{*}*Corresponding author: Aristotelis Tsirigos, Aristotelis.Tsirigos@nyulangone.org*

18 January 2024

19 **Abstract**

20 Self-supervised learning (SSL) automates the extraction and interpretation of histopathology features
21 on unannotated hematoxylin-and-eosin-stained whole-slide images (WSIs). We trained an SSL Barlow
22 Twins-encoder on 435 TCGA colon adenocarcinoma WSIs to extract features from small image patches.
23 Leiden community detection then grouped tiles into histomorphological phenotype clusters (HPCs).
24 HPC reproducibility and predictive ability for overall survival was confirmed in an independent clinical
25 trial cohort (N=1213 WSIs). This unbiased atlas resulted in 47 HPCs displaying unique and sharing
26 clinically significant histomorphological traits, highlighting tissue type, quantity, and architecture, es-
27 pecially in the context of tumor stroma. Through in-depth analysis of these HPCs, including immune
28 landscape and gene set enrichment analysis, and association to clinical outcomes, we shed light on the
29 factors influencing survival and responses to treatments like standard adjuvant chemotherapy and ex-
30 perimental therapies. Further exploration of HPCs may unveil new insights and aid decision-making
31 and personalized treatments for colon cancer patients.

32 **Keywords**

33 Colon cancer; Histopathology; Self-supervised learning; Overall Survival; Tumor microenvironment;
34 Bevacizumab.

35 Introduction

36 Traditionally, the diagnosis of colon cancer is confirmed by microscopic assessment of resection speci-
37 mens on hematoxylin and eosin-stained (H&E) slides by pathologists. For each patient, a personalized
38 treatment strategy is tailored through a multidisciplinary meeting, following guidelines consisting of risk
39 assessments based on clinicopathological characteristics, including the tumor-node-metastasis (TNM)
40 classification and additional biomarkers[1, 2, 3, 4]. However, due to an aging population and expo-
41 nential biomarker research, diagnosing and predicting the prognosis of colon cancer patients can be
42 time consuming, or complicated and resource-demanding, especially when incorporating screening for
43 mutational variants [2, 3, 5, 6].

44 In modern digital pathology, scanning H&E slides into high-resolution whole slide images (WSIs) has
45 enabled the applications of deep learning (DL)[7]. Deep convolutional neural networks, in particular,
46 have benefited the diagnostic process, initially by minimizing inter-rater disagreement and workload[7].
47 In colorectal cancer, supervised DL models also showed the ability to predict molecular pathways (i.e.
48 mutation density, microsatellite instability [MSI], chromosomal instability) and key mutations like *BRAF*
49 and *KRAS*[8, 9]. DL even has intriguing potential in predicting complicated prognostic outcomes such
50 as patient survival[10, 11]. Moreover, integrating multi-omic data with the associated H&E slides, i.e.
51 multimodal data integration, led to improvements in prognostic prediction on overall survival (OS) for
52 most cancer types[12].

53 Previous DL studies primarily focused on training models to extract features from WSIs under
54 supervision of potentially extensive and time consuming human-derived annotations on slide or pixel-
55 level, i.e. supervised learning[13, 8, 10, 12]. Self-supervised learning (SSL) on the other hand, has
56 gained significantly increasing attention for its capacity to automatically capture image features from
57 unlabeled data[9]. Applications of SSL models have demonstrated superior performance in various
58 cancer classification and survival prediction tasks compared to traditional supervised learning models[14,
59 15, 16, 17]. Barlow Twins, an SSL model designed to learn non-redundant image features, has several
60 advantages over other SSL learning models (e.g. contrastive learning models), including not requiring
61 extensive batch sizes nor asymmetry between the network "twins"[18].

62 Despite the efficacy in decision-making, DL models are often labeled as "black boxes," posing signif-
63 icant challenges in terms of interpretability. Supervised attention-based multiple instance learning is a

64 common interpretive method, enabling DL models to concentrate on informative segments within WSI
65 according to predefined training labels[19]. Another approach involves employing unsupervised cluster-
66 ing algorithms to organize extracted features into clinically relevant and interpretable clusters which
67 can be subsequently linked to diverse patient-related outcomes[20, 21, 17]. These clustering methods
68 offer significant advantages, including the prediction of various clinical outcomes, intuitive visualization
69 for pathologists, and interpretation and correlation with a range of molecular data.

70 Our objective is twofold: first, to automatically and reliably extract clinically-relevant histologic
71 patterns from WSIs, which can be interpreted by expert pathologists, and second, to investigate the
72 connections between these patterns and patient outcomes as well as molecular phenotypes across differ-
73 ent treatment groups within a large clinical trial for colon cancer. To achieve this, we applied an SSL
74 pipeline [17] involving the Barlow Twins encoder for feature extraction followed by a community de-
75 tection algorithm to construct an unbiased atlas of histomorphologic phenotype clusters (HPCs). This
76 algorithm was exclusively trained on public data from the colon adenocarcinoma cohort within The
77 Cancer Genome Atlas (TCGA) multi-institutional database[22]. Remarkably, the identified HPCs gen-
78 eralized well in unseen WSIs obtained from the clinical Bevacizumab-Avastin® adjuVANT (AVANT)
79 trial [23]. Subsequently, HPCs were linked to patient OS. An HPC-based classifier trained using TCGA
80 data for OS, demonstrated prognostic significance in the external validation of AVANT study, even
81 when considering key clinical and demographic factors typically employed in clinical settings. Notably,
82 by conducting comprehensive analyses of the distinct histomorphologic features of each HPC and their
83 associations with immune and genetic profiles, we provide insight into morphological and molecular
84 determinants of patient survival upon different treatments (e.g. standard-of-care adjuvant chemother-
85 apy and experimental targeted therapies). Exploring these features further could yield novel insights
86 into other histopathology diagnostics, supporting shared decision-making and advancing personalized
87 treatment options for colon cancer patients in the future.

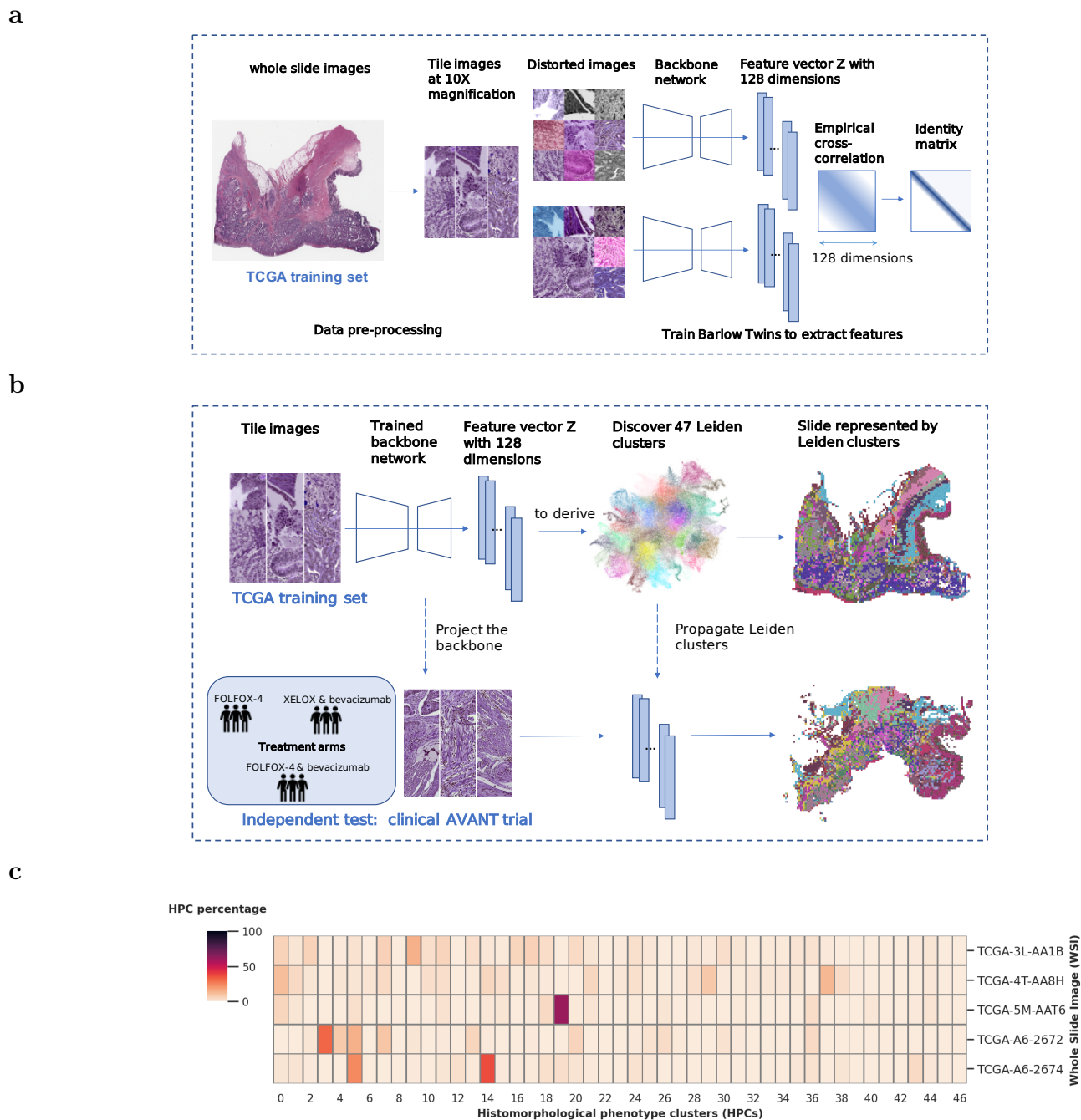


Figure 1: Overview of the Model Architecture: Training Barlow Twins and deriving Histomorphological Phenotype Clusters. (a) Training Barlow Twins with TCGA. WSIs from TCGA were processed to extract image tiles and normalize stain colors. The Barlow Twins network was employed to learn 128-dimensional z vectors from these image tiles. (b) Deriving HPCs. The tiles from TCGA were projected into z vector representations obtained from the trained Barlow Twins network. HPCs were defined by applying Leiden community detection to the nearest neighbor graph of z tile vector representations. Each WSI was represented by a compositional vector of the derived HPCs, indicating the percentage of each HPC with respect to the total tissue area. The Barlow Twins model and HPCs were then projected and integrated into the external AVANT trial. (c) Whole Slide Image Representation. The compositional HPC data represented the WSIs in the study. AVANT, Bevacizumab-Avastin® adjuvant trial. HPC, histomorphological phenotype cluster. TCGA, The Cancer Genome Atlas. WSI, whole slide image.

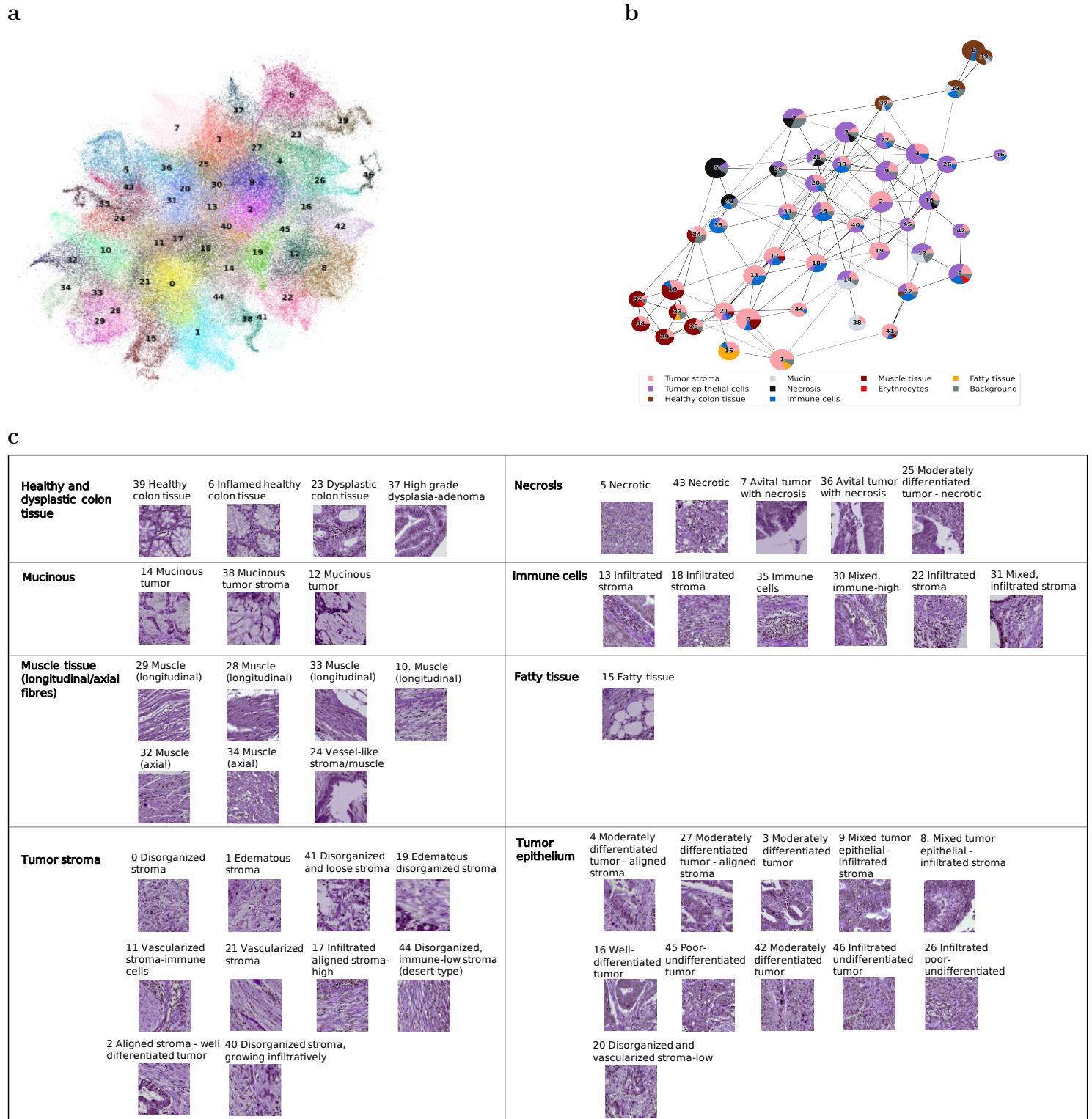


Figure 2: **Identification of HPCs in TCGA and subsequent classification into super-clusters** (a) UMAP showing 47 HPCs identified from the TCGA dataset, each scatter representing an image tile. (b) PAGA plot of HPCs. Each node represented an HPC with edges representing connections between HPCs based on their vector representation similarity. The pie chart of each node represented the tissue composition for each HPC. (c) Grouping of HPCs into super-clusters according to histopathology tissue similarities. Representative tiles for each HPC were labeled with ID and a brief description. HPC, histomorphological phenotype cluster. PAGA, partition-based abstraction graph. TCGA, The Cancer Genome Atlas. UMAP, uniform manifold approximation and projection plot

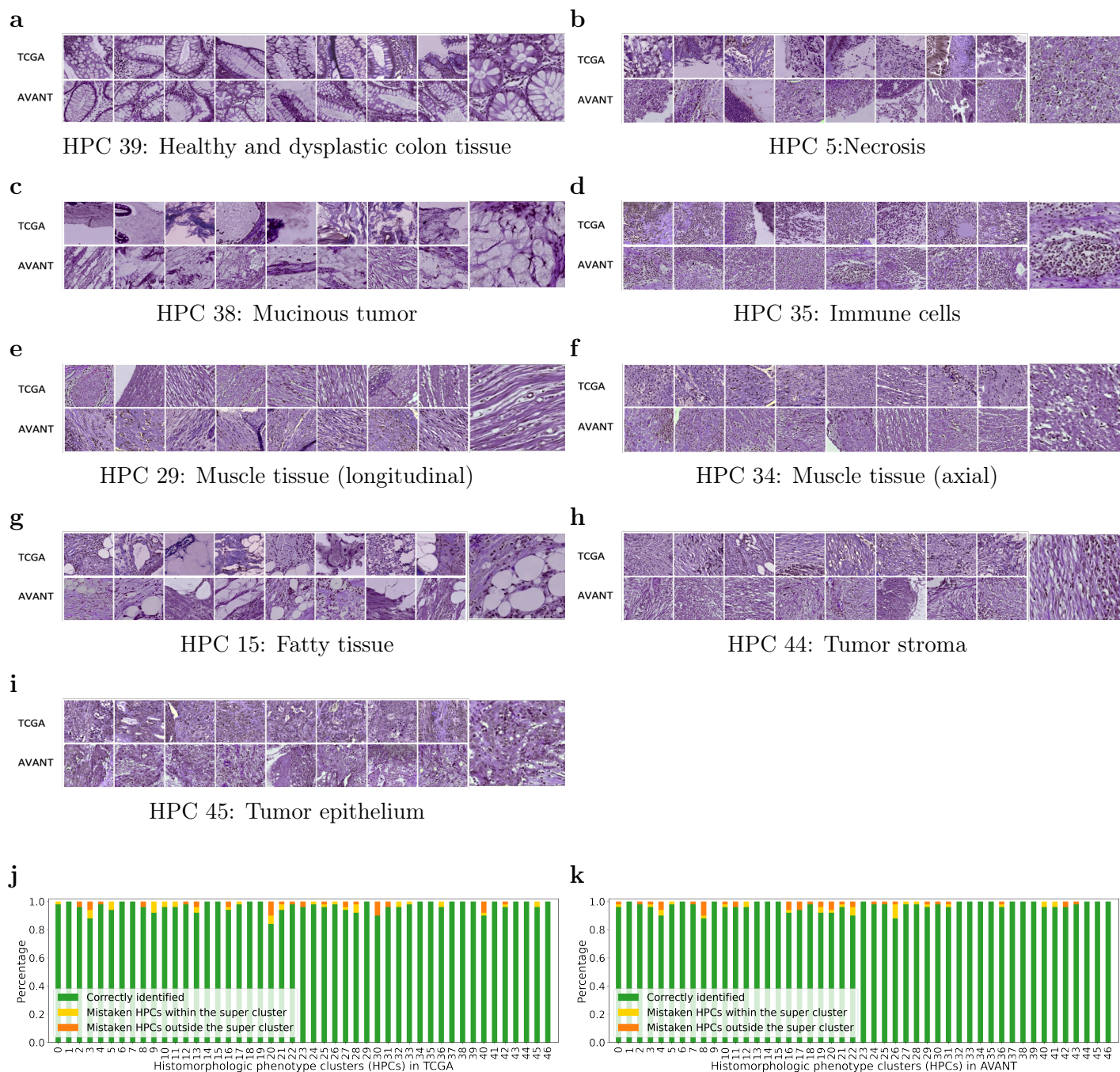


Figure 3: **Verification of HPCs in the TCGA training set and the external AVANT trial (a-i)** Example tiles from TCGA (upper row) and external clinical AVANT trial (lower row) showcase the eight super-clusters with a zoomed-in representative tile. Notably, the muscle tissue super-cluster is further divided into longitudinal and axial subgroups (j,k) Stacked bar plots illustrate instances of misclassification for each HPC in TCGA training set and AVANT external test set. Green bars represent the percentage of correctly identified odd clusters, yellow bars indicate misclassifications within the tested HPC's super-cluster, and orange bars show misclassifications outside the super-cluster. HPC, histomorphological phenotype cluster. TCGA, The Cancer Genome Atlas. AVANT, Bevacizumab-Avastin® adjuvant trial.

88 Results

89 Self-supervised learning of WSI features using the multi-institutional TCGA 90 dataset

91 We trained the self-supervised algorithm using data exclusively from the TCGA colon adenocarcinoma
92 (TCGA-COAD) set, eliminating the need for annotations by pathologists (Figure 1). A total of 435
93 WSIs (428 patients) obtained from the TCGA-COAD dataset (see Methods: Study population for
94 details) was first divided into smaller image patches (224-by-224 pixels), also known as image tiles, at a
95 magnification level of 10x (Figure 1a) (see Online Methods: Data pre-processing for details). To identify
96 features on these patches, we trained a SSL Barlow Twins feature extractor using a random subset of
97 tiles (Figure 1a) (see Methods: Extracting image features using Barlow Twins for details). The Barlow
98 Twins was trained with the objective function to evaluate the cross-correlation matrix between the
99 embeddings (feature vector z) of two identical backbone networks, which were fed distorted variants of
100 a batch of image tiles. The objective function was optimized by minimizing the deviation of the cross-
101 correlation matrix from the identity matrix. This led to increased similarity among the embedding of z
102 vectors of the distorted sample versions, while reducing redundancy among the individual components
103 of these vectors. As a result, each tile was described as a vector of 128 extracted features that can
104 subsequently be used to group tiles into clusters by similarity.

105 Construction of an unbiased atlas of histologic patterns through community 106 detection

107 We applied Leiden community detection algorithm to derive HPCs, the clusters with similar histologic
108 patterns (Figure 1b) (see Methods: Identification of Histomorphological Phenotype Clusters (HPCs)
109 for details). The process began by first projecting the trained Barlow Twins onto the entire TCGA-
110 COAD dataset, extracting 128-dimensional feature representations for each image tile. Subsequently,
111 we utilized Leiden community detection on a nearest neighbor graph constructed from these tile vector
112 representations (Figure 1b). Tiles with similar vector representations were clustered into a group and
113 assigned a specific HPC ID number. The optimization of the Leiden configuration was achieved through
114 an unsupervised process (see Methods: Identification of Histomorphological Phenotype Clusters (HPCs)

115 for details, Supplementary Figure 1a), resulting in the identification of a total of 47 HPCs, visually rep-
116 resented in a dimensionality reduction plot (Uniform Manifold Approximation and Projection; UMAP
117 plot) (Figure 2a).

118 As external dataset, we analyzed a total of 1213 colon cancer patients with pathology diagnostic H&E
119 WSIs (one WSI per patient), a subset of the clinical AVANT trial[23, 24] (see Online Methods: Study
120 population for details). We harnessed the optimized SSL Barlow Twins model to generate embeddings
121 of the unseen AVANT WSI tiles. The assignment of identified HPCs to the unseen AVANT was achieved
122 using the K-nearest neighbors approach. The HPC label of each tile in the AVANT data was determined
123 based on majority votes from its K-nearest neighbors in the TCGA training set (Figure 1b). As a
124 result, we obtained comprehensive visual representations of the WSIs where the WSI tiles are colored
125 by their corresponding HPC (Figure 1b). Additionally, we were able to capture the characteristics and
126 heterogeneity of WSIs using the compositional data derived from the HPCs, i.e. the percentage of the
127 area on a WSI covered by each HPC, thus facilitating downstream analyses and modeling (Figure 1c).

128 **Histopathological assessment and characterization of HPCs**

129 Each HPC underwent histopathological analysis on a randomly selected set of 32 tiles per cluster within
130 TCGA, independently evaluated by two pathologists (ASLPC and JHJMvK) and a researcher (MP)(see
131 Online Methods: Interpretation of HPCs for details). Tissue types, as observed on the tiles, were de-
132 scribed with specific attention to tumor epithelium, tumor stroma and immune cells. Other unique
133 histopathological features or patterns, such as tumor differentiation and stromal organization, were
134 noted as well. All present tissue types were scored in percentages (Supplementary Table 1) and de-
135 picted using pie charts (Figure 2b). We plotted the interconnections of 47 HPCs using partition-based
136 graph abstraction (PAGA)[25], with the pie charts reflecting their tissue compositions (Figure 2b).
137 Interestingly, distinct larger groups of clusters, or "super-clusters", could be observed based on the
138 similarity of tissue composition, interconnectedness, and topology of HPCs in the PAGA plot (Figure
139 2b).

140 In total, we identified eight super-clusters: (1) healthy and dysplastic colon tissue, (2) necrosis,
141 (3) mucinous areas, (4) immune cells, (5) muscle tissue (longitudinal/axial), (6) fatty tissue, (7) tu-
142 mor stroma, and, (8) tumor epithelium, in no particular order, formed by groups of HPCs shown in
143 Figure 2c. Common histopathological characteristics were noted among HPCs within each designated

144 super-cluster, while HPCs encompassing varied tissue types across multiple super-clusters were often
145 situated at their intersections. For instance, HPC 12, containing not only tumor epithelium but also
146 mucinous tumor, was located between HPCs belonged to the two super-clusters of mucinous tumor
147 and tumor epithelium in the PAGA plot. Moreover, HPC 23 marked by dysplastic colon tissue formed
148 a bridge between the healthy colon tissue HPC 39 and the tumor epithelium-containing super-cluster
149 HPCs, suggesting a chronological pathogenesis. In summary, the derived HPCs displayed distinctive
150 histopathologic characteristics. Moreover, HPCs located in close proximity on the UMAP and PAGA
151 plot, based on the extracted features, demonstrated common traits, hinting at potential pattern rela-
152 tionships, mixed phenotypes, or pathogenic trajectories.

153 **Assessment of HPC consistency within and across TCGA and AVANT co-** 154 **horts**

155 Although SSL methods have been applied recently in histopathology, there is usually no systematic
156 analysis of consistency of the histologic patterns discovered by these methods within and across datasets
157 [15, 20]. Here, we address this potential pitfall by incorporating several qualitative and quantitative
158 assessments.

159 First, qualitative assessment was conducted to evaluate the within-cluster and between-cluster het-
160 erogeneity of 47 HPCs derived in TCGA-COAD. Based on 32 randomly selected tiles from each HPC
161 in the TCGA-COAD, three experts (ASLPC, JHJMvK, and MP) independently assessed each HPC
162 by comparing tissue type quantity and architectures (histopathological assessment procedure stated
163 above). Overall, all raters reached the general consensus that there was a noteworthy level of within-
164 cluster morphological similarity and a significant diversity among the 47 HPCs (Figure 3 [a-i]), although
165 phenotypic similarities varied across HPCs, implying that some HPCs may appear more similar than
166 others. To delve deeper into the within-cluster and between-cluster heterogeneity, we carried out quanti-
167 tative objective blinded tests within TCGA and AVANT tiles separately. This was to ascertain whether
168 the morphological patterns identified by each HPC could also be recognized by human experts. In this
169 test, the assessor (MP) was shown three groups of five tiles each. Two groups were from the same
170 HPC, and the third was from a randomly selected other HPC, also called the "odd HPC". The assessor
171 was required to identify the "odd HPC" (Supplementary Figure 2a, see Online Methods: Pathologist

172 assessment of HPCs, for details). Each of the 47 HPCs underwent 50 tests to determine the success
173 rate. Within TCGA, we found that 17 out of the 47 HPCs achieved 100% identification rate, while
174 the remaining 30 HPCs had a correct identification percentage ranging from 84% to 98%. Similarly,
175 within in AVANT, 17 out of 47 HPCs achieved the perfect accuracy, while the rest had accuracy ranging
176 from 88% to 98% (Figure 3j). In general, HPCs in close proximity to each other in the PAGA plot or
177 belonging to the same super-cluster were more prone to erroneous assignment.

178 To evaluate the effectiveness of transferring morphological patterns from the TCGA to the external
179 AVANT test set, three experts (ASLPC, JHJMvK, and MP) independently reviewed a randomly chosen
180 set of 32 tiles from the TCGA-COAD subset and another 32 tiles randomly selected from the AVANT
181 trial. This qualitative comparison concluded a remarkable resemblance between the TCGA and AVANT
182 tiles within their respective HPCs (Figure 3 [a-i]). In comparing the objective test results from TCGA
183 and AVANT, we found an 80% overlap in the misclassified HPCs between the two datasets and 65%
184 overlap in correctly classified HPCs. These results indicate that the robust morphological features
185 extracted from the training set can be effectively transferred to an independent unseen test set.

186 **HPC-based classifier was associated to OS in patients treated with standard-** 187 **of-care and AVANT-experimental treatment**

188 We explored the prognostic significance of HPCs on OS. The OS prediction model was developed
189 within TCGA-COAD (see Online Methods: Identification of Histomorphological Phenotype Clusters
190 (HPCs), for details). For external validation, we utilized the control group from the AVANT trial
191 who had only received standard adjuvant chemotherapy (i.e. FOLFOX-4). The AVANT trial aimed
192 to investigate whether combining bevacizumab, a humanized anti-vascular endothelial growth factor
193 (VEGF) monoclonal antibody, with standard chemotherapy would improve survival among colon can-
194 cer patients[26, 23]. The trial had three treatment arms: FOLFOX-4, bevacizumab+FOLFOX-4, beva-
195 cizumab+XELOX. The study was prematurely terminated due to the adverse effect in patient survival
196 associated with bevacizumab[23]. Given the unique bevacizumab experimental treatment and its adverse
197 effects, we hypothesized that the survival model trained on TCGA-COAD patients may not generalize
198 well in the AVANT bevacizumab-treated group. We referred to our source population, represented by
199 the TCGA-COAD, as the "standard-of-care group", in contrast to the unique bevacizumab treatment

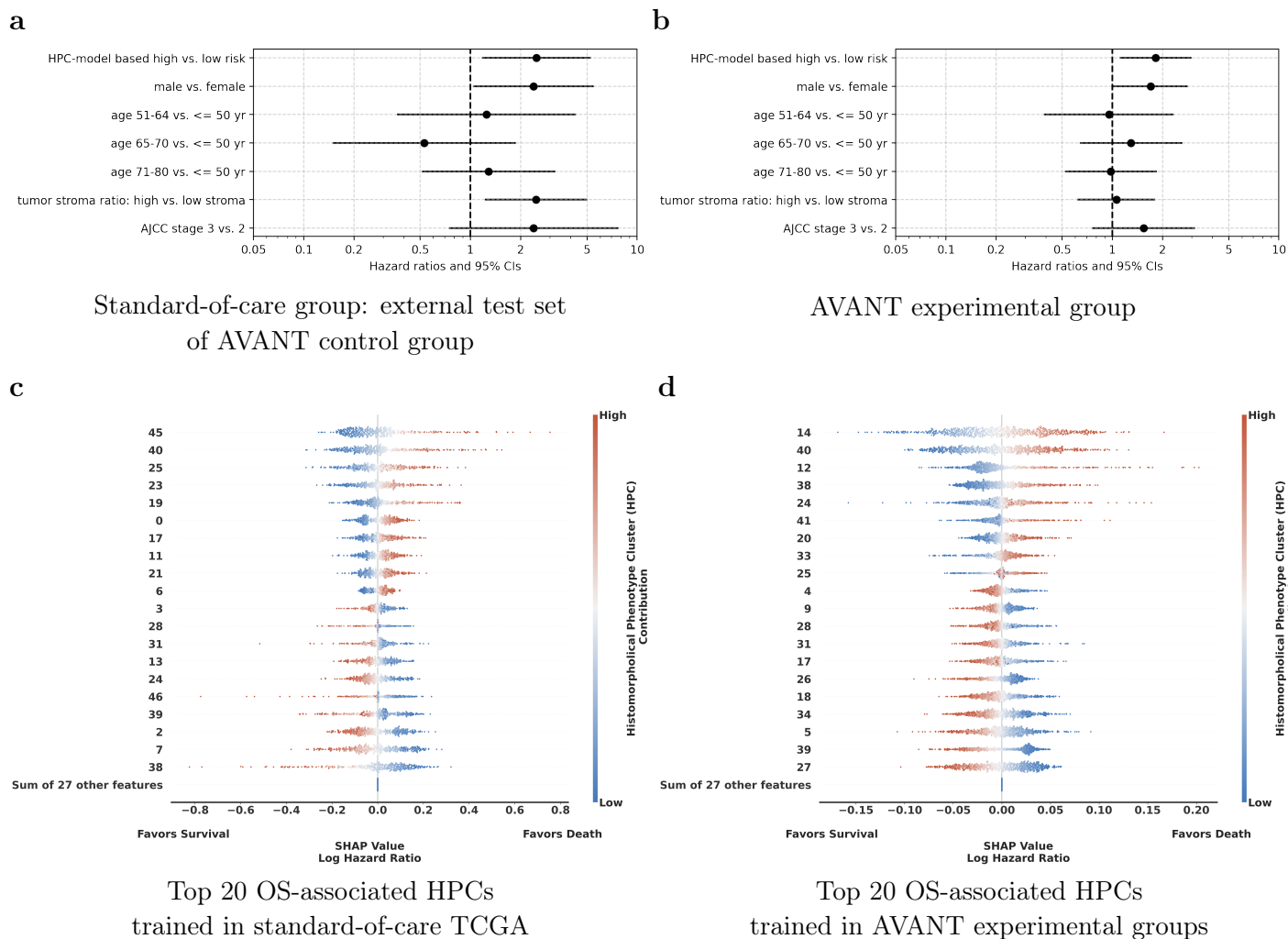


Figure 4: HPC-based classifier was associated with OS in patients treated with standard-of-care and AVANT-experimental treatment. (a) Ordinary Cox regression for OS, incorporating the HPC-based risk classifier, along with sex, age categories, tumor-stroma ratio, and AJCC TNM staging, was conducted within the external test set of the AVANT control group. The HPC model-based classifier stands as an independent prognostic factor (HR 2.50, 95% CI 1.18-5.31) for OS. (b) Ordinary Cox regression for OS, incorporating the HPC-based risk classifier, along with sex, age categories, tumor-stroma ratio, and AJCC TNM staging, was conducted within the AVANT experimental group. The HPC model-based classifier stands as an independent prognostic factor (HR 1.82, 95% CI 1.11-2.99) for OS. (c and d) The SHAP summary plots depict the relationship between the center-log-transformed compositional value of an HPC and its impact on death hazard prediction. The color bar indicates the relative compositional value of an HPC, with red indicating higher and blue indicating lower composition. Higher compositions of the top 10 HPCs were associated with worse OS, while higher compositions of the bottom 10 HPCs were linked to improved OS. AJCC TNM, American Joint Committee on Cancer tumor-node-metastasis classification. AVANT, Bevacizumab-Avastin® adjuvant trial. HPC, histomorphological phenotype cluster. OS, overall survival. SHAP, SHapley Additive exPlanations. TCGA, The Cancer Genome Atlas.

200 in the AVANT trial. We then opted to validate the OS prediction model, trained on TCGA-COAD
201 data, primarily on AVANT patients who exclusively received standard FOLFOX-4 chemotherapy. This
202 subset is henceforth referred to as the "AVANT control group", serving as an independent test set for
203 validation.

204 We modeled HPCs on OS using Cox regression with L2 regularization trained within the TCGA-
205 COAD incorporated all 47 HPCs as predictors. The model was optimized through five-fold cross-
206 validation (CV) on the TCGA training set (see Online Methods: Identification of Histomorphological
207 Phenotype Clusters (HPCs), for details). The optimized regularized Cox model was then tested in the
208 independent test set of the AVANT control group. We observed the test set c-index of 0.65 (bootstrap
209 95% confidence interval [CI] 0.55-0.74) (Supplementary Figure 3b). The HPC-based classifier (i.e. high
210 risk versus low risk) was determined by the median predicted hazard obtained in the TCGA-COAD.
211 The HPC-based model also outperformed a clinical baseline model trained on age, sex, tumor-stroma
212 ratio (TSR), and AJCC stage (Supplementary Figure 3c). To investigate whether HPC-based classifier
213 provides additional prognostic value to the existing important clinical predictors, a regular multivariable
214 Cox regression was fitted within the external AVANT control test set. The model included HPC-based
215 classifier as well as important clinical and demographic variables (Figure 4a). Notably, the HPC-based
216 risk classifier demonstrated significance as an independent prognostic factor (hazard ratio [HR] 2.50,
217 95% CI 1.18-5.31), along with male sex (HR 2.42, 95% CI 1.07-5.47) and the TSR (HR 2.49, 95% CI
218 1.23-5.04). The 20 most important HPCs associated to OS were summarized using the interpretable
219 SHapley Additive exPlanations (SHAP) (Figure 4c).

220 Harnessing the well-defined experimental protocols in AVANT, we were granted the unique oppor-
221 tunity to examine the influence of HPCs on colon cancer OS in the bevacizumab treatment groups
222 (i.e. bevacizumab+FOLFOX-4 or bevacizumab+XELOX). Given the proven comparable therapeutical
223 efficacy of FOLFOX-4 and XELOX [26, 27, 28], we consolidated the bevacizumab+FOLFOX-4 and
224 bevacizumab+XELOX cohorts into a unified "AVANT-experimental group". Similar to the analysis
225 stated above, we trained Cox regressions with L2 regularization encompassing all 47 HPCs within the
226 AVANT-experimental patients using 5-fold CV (see Online Methods: Identification of Histomorpho-
227 logical Phenotype Clusters (HPCs) for details). The HPC-based classifier remained of independent
228 prognostic value (HR 1.82, 95% CI 1.11-2.99) after adjusting for age, sex, tumor staging, and TSR
229 (Figure 4b). The top 20 most influential HPCs on OS prediction were shown in the SHAP summary

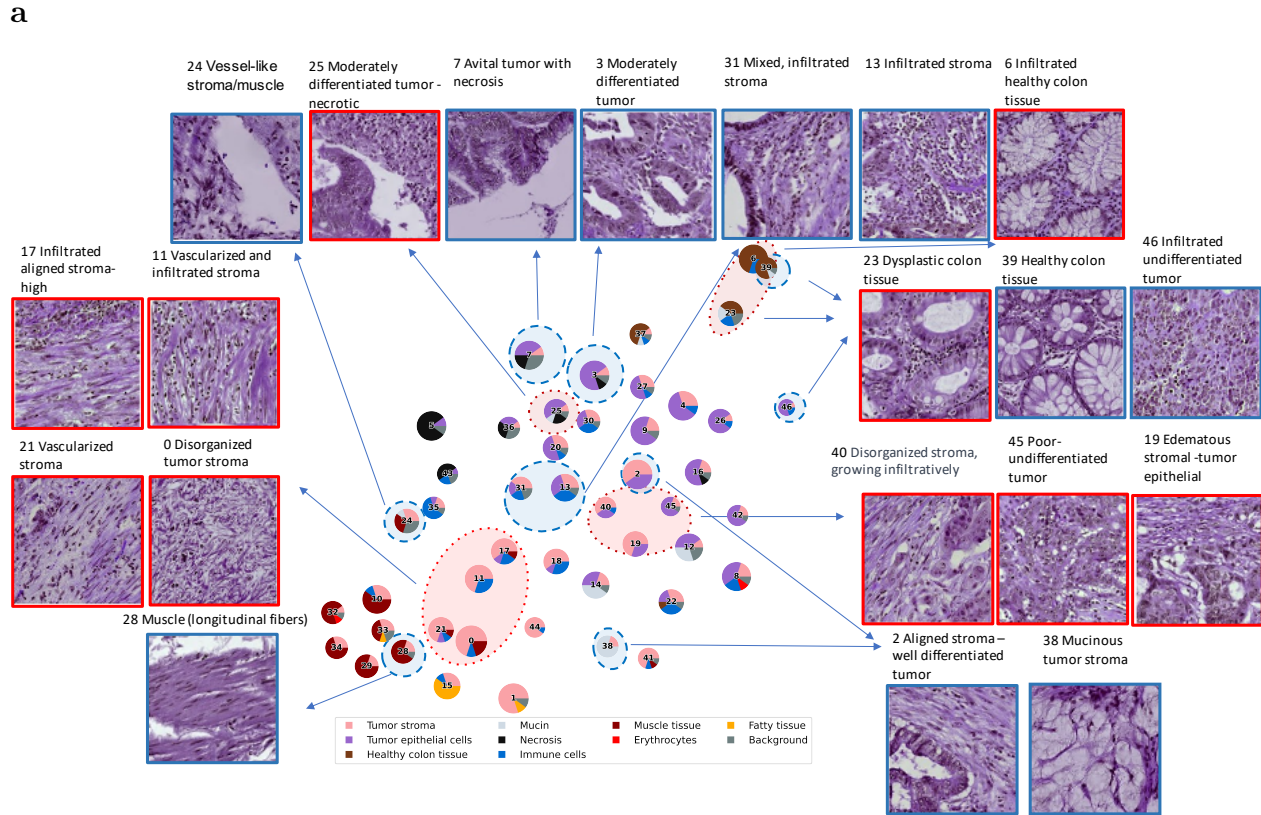
230 plot (Figure 4d).

231 **Pathological assessment of OS-associated HPCs in the standard-of-care and** 232 **AVANT-experimental group groups**

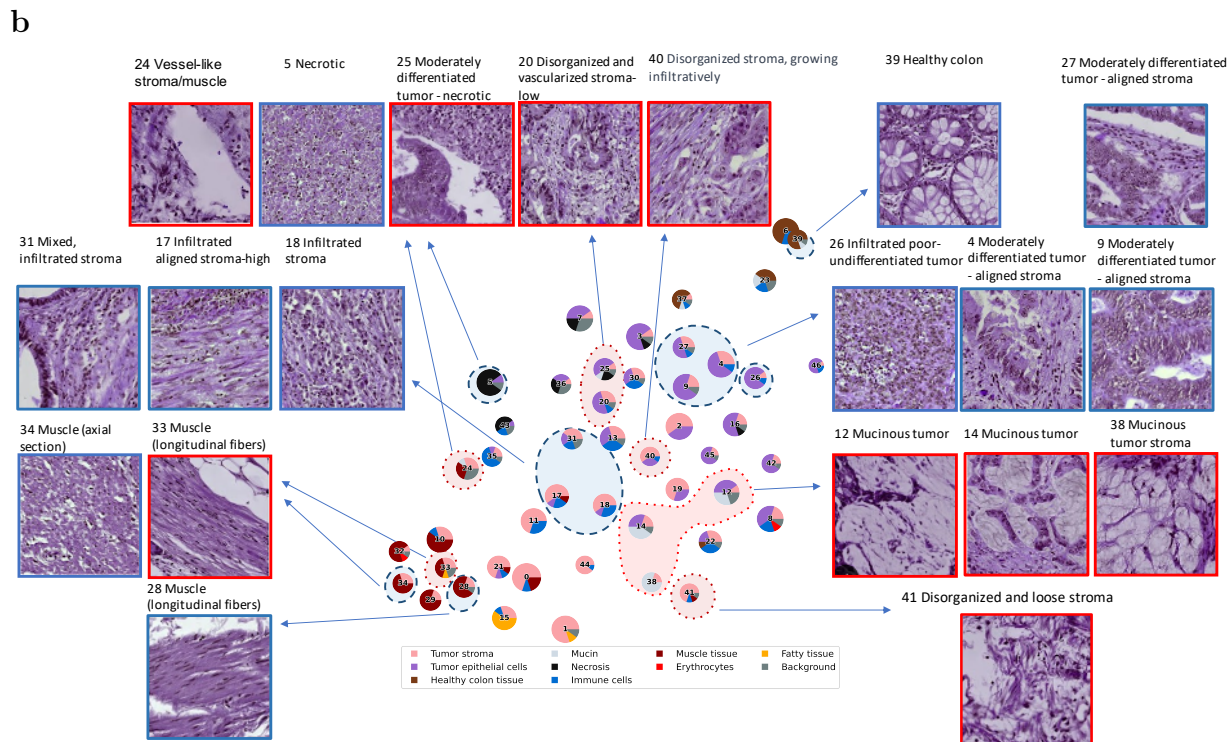
233 We highlighted the top 20 most influential HPCs on OS prediction reflecting the SHAP summary plot
234 (Figure 4c, 4d) in the PAGA plots for the standard-of-care and AVANT-experimental groups (Figure
235 5). The survival-favorable HPCs were highlighted in a shade of red and the survival-unfavorable HPCs
236 were highlighted in blue. Preliminary findings showed that HPCs containing proportionally more healthy
237 colon tissue or immune cells appeared associated with an improved OS, and HPCs comprising mucinous
238 tumor, tumor stroma, and poor-to-undifferentiated tumor epithelium were associated with worse OS in
239 both groups.

240 The healthy colon tissue-containing HPC 39 was among the top survival-favorable HPCs indicated by
241 larger SHAP values in both groups (Figure 4c, 4d). In the standard-of-care group, HPC 23 characterized
242 by dysplastic and low grade tumor epithelium and HPC 6 marked by stroma-infiltrated healthy colon
243 tissue indicating inflammation, were associated with a worse OS. HPC 31, predominately composed of
244 immune cells, was associated with an improved OS in both treatment groups. A similar association was
245 also noted for immune-mixed HPC 13, which is part of the immune super-cluster, in the standard-of-
246 care group (Figure 5a) as well as HPC 18 (aligned stroma-immune cells) and HPC 17 (aligned stroma
247 with immune component) in the AVANT-experimental group (Figure 5b). In the AVANT-experimental
248 group, the mucinous super-cluster (HPCs 12, 14 and 38) was associated with a poor survival (Figure
249 5b), while conversely, HPC 38 (mucinous tumor stroma) led to a better survival in the standard-of-care
250 group (Figure 5a)

251 Upon closer examination, we noted that the algorithm captured a distinction in stroma organization
252 within the stromal tissue presented in the tumor stroma and tumor epithelium super-clusters. HPCs
253 in these two super-clusters all contained some component of stromal tissue. However, HPCs with
254 disorganized or heterogeneous tumor stroma with neovascularization (HPC 40 in both groups; 0, 11 and
255 21 in standard-of-care, and 41 in the AVANT-experimental group) were associated with a poor survival,
256 whereas aligned and organized tumor stromal "strands" were often observed among the top survival-
257 favorable HPCs (HPC 2 in the standard-of-care and HPC 27 in the AVANT-experimental group).



Top 20 OS-related HPCs in the standard-of-care group



Top 20 OS-related HPCs in the AVANT-experimental group

Figure 5: **PAGA plots highlighted with important HPCs related to OS in the standard-of-care and experimental treated group** (a) Standard treated group: HPCs colored in the red are linked to worse survival and HPCs colored in blue are linked to better survival. (b) AVANT-experimental treated group: HPCs colored in the red are linked to worse survival and HPCs colored in blue are linked to better survival. AVANT, Bevacizumab-Avastin® adjuvant trial. HPC, histomorphological phenotype cluster. PAGA, partition-based graph abstraction.

258 Moreover, the tumor differentiation grade was another parameter correlating with HPCs and their
259 impact on OS. Poor-to-undifferentiated tumor epithelium, e.g. HPC 45, in the standard-of-care group,
260 was linked to a worse survival, while well-to-moderately differentiated tumor led to an improved sur-
261 vival (e.g. HPCs 3 in the standard-of-care group and HPC 4 in the AVANT-experimental group). A
262 unique pattern was furthermore observed in survival-favorable HPCs 46 (standard-of-care group) and 26
263 (AVANT-experimental group), which was characterized by a predominance of poor-to-undifferentiated
264 tumor epithelium but accompanied by a notable influx of immune cells.

265 Additional findings were related to the survival-favorable HPC 7 (avital tumor epithelium) in the
266 standard-of-care group (Figure 5a) and the positive association between necrosis-dominated HPC 5
267 and better survival in the AVANT-experimental group (Figure 5b). The associations between HPCs
268 containing muscle tissue (e.g. HPC 24, 33 and 34) and survival were generally inconsistent, possibly due
269 to the similarity of muscle fibers and tumor stroma, caused for instance by the organization of muscle
270 fibers and vascularization.

271 **Outcome-associated HPCs are linked to diverse immune features in the tumor** 272 **microenvironment**

273 Spearman correlation coefficients were calculated between the top 20 survival-related HPCs on one hand,
274 and the TCGA immune landscape on the other hand (see Methods for details). The correlation heatmap
275 was plotted with bi-directional hierarchical clustering (Figure 6a). Interestingly, in the standard-of-care
276 group (Figure 6a), HPCs 0, 11, 17 and 21, all part of the phenotypic tumor stroma super-cluster,
277 were identified by the genotypic immune analysis as having a positive correlation with the stroma-
278 high category. Moreover, their SHAP values indicated an positive association with worse survival.
279 Conversely, HPCs 13 and 31 in the immune cell super-cluster were correlated with higher leukocyte
280 fraction. Survival prediction model suggested the immune cell super-cluster was in general associated
281 with a better survival. Further anticipated findings included the validation of HPCs 2 and 24, marked
282 by stroma-high tiles, through immune feature correlation within the stroma high category.

283 In the AVANT-experimental group (Figure 6b), survival-favorable HPCs 5, 17, 31, 18 correlated
284 with an increased leukocyte fraction. Notably, HPCs 17 and 31 aligned with an elevated immune cell
285 composition (Figure 5b). Additionally, HPCs 17 and 18 were also associated with a higher expression of

286 stroma, which was consistent with the observed stroma-high morphology (Figure 5b). On the contrary,
287 survival-unfavorable HPCs 14, 40 and 20 exhibited higher genomic instability. For instance, HPCs 40
288 and 20 were positively correlated with homologous recombination defects, intratumor heterogeneity,
289 and HPC 14 was positively linked to nonsilent mutation rate, single nucleotide variants and indel
290 neoantigens. Although HPC 14 also showed a positive correlation with the leukocyte fraction, a more
291 pronounced association with genomic instability through multiple pathways seemed to play a greater
292 role in its negative impact on OS.

293 The resulting correlations with immune landscape data aligned with the observed morphologies of
294 HPCs, particularly in stromal and immune features. Furthermore, the data suggest a potential role in
295 genomic instabilities within the AVANT-experimental group. Taken together, these results demonstrate
296 that HPCs can capture the remarkable heterogeneity of the tumor microenvironment.

297 **Outcome-associated HPCs are linked to oncogenic pathways and bevacizumab's** 298 **mechanism of action**

299 Next, we performed gene set enrichment analysis (GSEA) to discern associations between top OS-
300 related HPCs from both the standard-of-care and AVANT-experimental groups and key cancer hall-
301 mark pathways (Figure 6c and d). In the AVANT-experimental cohort, survival-related HPCs showed
302 striking alignment with the enrichment observed in oncogenic hallmark pathways (Figure 6d), which
303 such alignment was overall much less pronounced in standard-of-care group (Figure 6c). Still, in the
304 standard-of-care group, pathways encoding epithelial-to-mesenchymal transition, leading to an increased
305 tumor-stromal percentage, were enriched in survival-unfavorable HPCs 11, 17, 40 and 19. HPCs related
306 to inflammatory response pathways showed primarily positive associations with OS, e.g. with HPCs 13
307 and 31 related to better survival.

308 In the AVANT-experimental group (Figure 6d), we observed a strong correlation between hierarchi-
309 cal clustering based on oncogenic enrichment scores and survival-related HPCs. Several HPCs exhibited
310 enrichment in pathways that potentially be specific to bevacizumab through its target of VEGFa ex-
311 pression and *KRAS* signaling-up pathway. HPC 5, characterized by necrosis, was linked to elevated
312 VEGFa expression ($\rho=0.163$, $P=0.005$), indicating patients with higher pre-treatment necrosis levels
313 may benefited from the bevacizumab treatment. HPC 27, 18, and 31 were associated with enriched

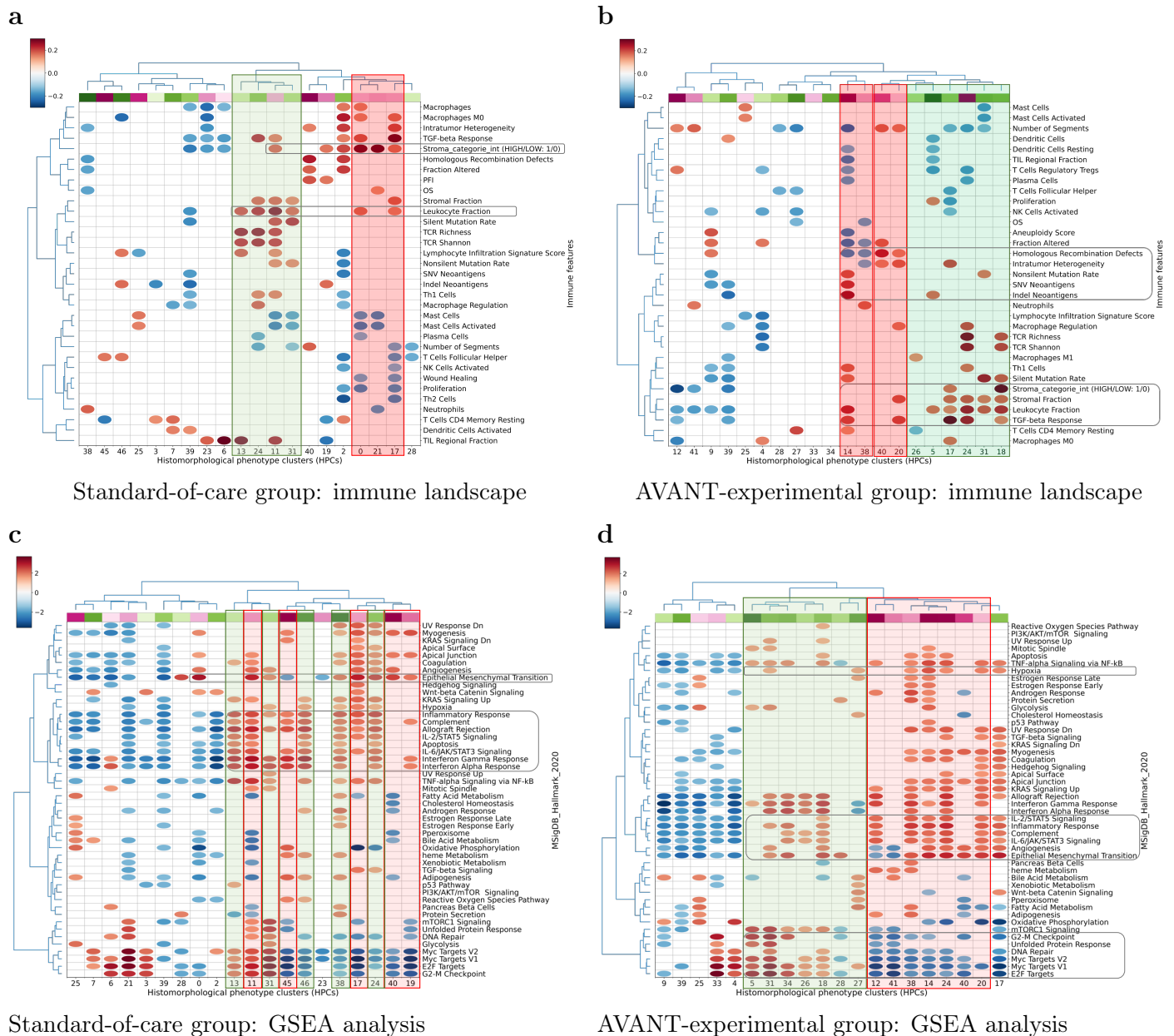


Figure 6: Survival-associated HPCs in relation to immune and genetic profile. (a) Standard-of-care group: Spearman's correlations between top 20 OS-related HPCs and immune landscape features. HPCs (columns of the matrix) were colored according to the beta-coefficients estimated from the optimized regularised Cox regression, with red indicating HPCs related to worse survival and green indicating HPCs related to better survival. The color bar at the upper left corner indicates the value of correlation coefficients with red denoting positive and blue denoting negative correlations. (b) AVANT-experimental treated group: Spearman's correlations between top 20 OS-related HPCs and immune landscape features. (c) Standard-of-care group GSEA between the top OS-related HPCs and major cancer hallmark pathways. HPCs (columns of the matrix) were colored according to the beta-coefficients estimated from the optimized regularised Cox regression, with red indicating HPCs related to worse survival and green indicating HPCs related to better survival. The color bar at the upper left corner indicates the value of the correlation coefficients with red denoting enrichment and blue denoting underrepresentation in a gene pathway. (d) AVANT-experimental treated group GSEA for the top 20 OS-related HPCs. AVANT, Bevacizumab-Avastin® adjuvant trial. GSEA, gene set enrichment analysis. HPC, histomorphological phenotype cluster. OS, overall survival.

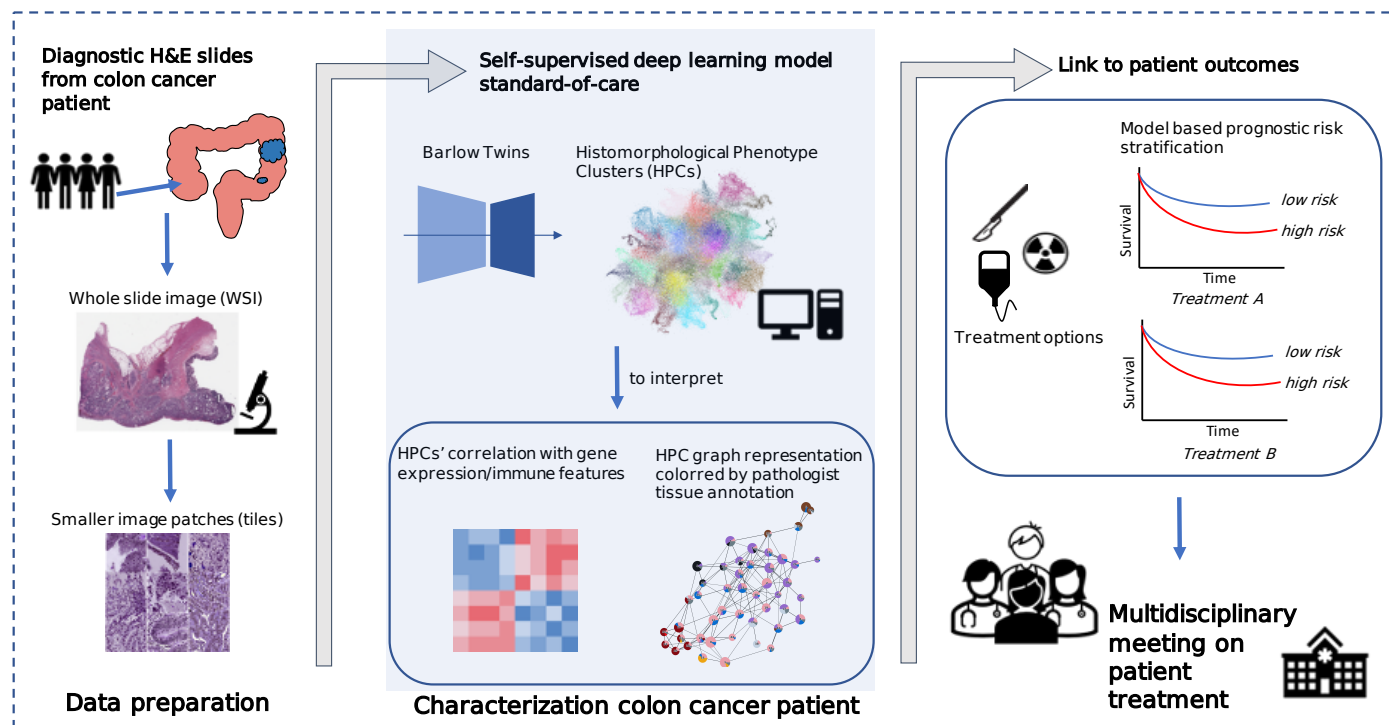


Figure 7: **Clinical application of AI-derived HPCs in prediction of patient outcomes.** The clinical algorithm consists of three key stages: data preparation, cancer patient characterization, and AI-supported multidisciplinary treatment meetings. Data preparation involves collecting histopathology WSIs, segmenting them into small image tiles. Patient characterization encompasses SSL model training, yielding HPCs via clustering. HPCs are easily interpretable by pathologists, linkable to omic data. Most importantly, HPCs are valuable for predicting diagnosis, patient outcomes, and treatment responses. In treatment-related outcomes, AI-predicted high/low risk groups aid multidisciplinary meetings, enabling personalized treatment plans by oncologists, pathologists, and physicians. AI, artificial intelligence. HPC, histomorphological phenotype cluster. SSL, self-supervised learning, WSI, whole slide image.

314 hypoxia (HPCs 31, 27) and angiogenesis (HPCs 18, 31), and unfolded protein (HPCs 31, 1, 5) path-
 315 ways which involve the VEGFa gene. In addition, other survival-favorable HPCs may not be specific to
 316 bevacizumab but related to the standard cytotoxic chemotherapy of XELOX and FOLFOX-4. Survival-
 317 unfavorable HPCs (12, 38, 14, 24, 20) were linked to the *KRAS* signaling-up pathway, which may have
 318 a negative impact on the prognosis of patients treated with FOLFOX. Certain survival-favorable HPCs
 319 exhibited enrichment in pathways related to cell cycle regulation, signaling, DNA repair, and growth,
 320 including G2/M checkpoint (34, 31, 5), E2F targets (5, 31, 34, 26, 18), Myc targets (5, 31, 34, 26, 18),
 321 and mTORC1 signaling (5, 31, 34, 26, 18), DNA repair (18, 31). In contrast, survival-unfavorable HPCs
 322 demonstrated depletion in these pathways.

323 Discussion

324 In this study, we derived and independently validated a total of 47 distinct HPCs that were extracted
325 from colon cancer H&E WSIs using a self-supervised algorithm. These HPCs possess distinctive histo-
326 morphologic features carefully identified and assessed by the pathologists and were also linked several
327 immune features and oncogenic pathways. The HPCs showed state-of-the-art performance on OS pre-
328 diction. Furthermore, the HPC-based risk classifier was an independent prognostic factor after adjusting
329 for important clinical and demographic variables, suggesting additional insight beyond the current clinical
330 prognostication. The unique AVANT trial enabled us to endeavor in identifying possible mechanisms
331 of response to bevacizumab and standard chemotherapy using the HPCs.

332 Moreover, we hereby emphasize the importance of the tumor microenvironment, or tumor stroma,
333 and its effect on survival. Tumor stroma is composed of extracellular matrix, vasculature, immune
334 cells and cancer-associated fibroblasts, forming a complex and close interaction with tumor epithelial
335 cells[29, 30]. Subject to increasing research the past decades, this dynamic entity has been found to
336 modulate tumor behavior through its cross-talk, and ultimately influence patient-related outcomes.
337 Specifically, regarding the amount of stroma and stromal architecture, i.e. alignment or categorization
338 of the desmoplastic reaction, and immune infiltrate in the stroma, our results corroborate previous
339 literature [31, 24, 32, 33, 34, 35].

340 We identified common histopathological patterns associated with survival as observed in both the
341 standard and bevacizumab-treated group. In line with our results, immune cells (e.g. HPCs 13, 31)[36]
342 and aligned stroma-low tumors (e.g. HPCs 2, 27)[32, 31] were associated with better survival, while
343 poor-to-undifferentiated tumor epithelium (e.g. HPC 45) or mucinous tumor epithelium (e.g. HPCs 12,
344 14) [2, 3], and disorganized stroma-high tumors (e.g. HPCs 40, 0)[32, 31] were linked to worse survival.
345 This pathological phenotype correlated with the corresponding genetic immune profile (e.g. increased
346 leukocyte fractions correlated with HPCs 13 and 31; and a stroma-high category was see in HPCs 0,
347 21, 17, 11) and enrichment in oncogenic pathways (e.g. epithelial-to-mesenchymal transition pathway,
348 contributing to tumor stroma amounts[29], correlated with HPCs 17 and 11). We also observed an
349 association, though imperfect, between mucinous tumor, poor-to-undifferentiated tumor epithelium, and
350 survival. One explanation may arise from the absence of contextual information in small images. The
351 differentiation between well-differentiated and undifferentiated, or adenocarcinoma and more mucinous

352 tumor types, is established based on whether each tissue type constitutes more than 50% of the total
353 tumor, underscoring the importance of considering the overall context[3].

354 Another interesting discovery emerges from the survival-favoring HPCs 26 (AVANT-experimental
355 group) and 46 (standard-of-care group). These HPCs contain primarily poor-to-undifferentiated tumor
356 epithelium but with a high influx of immune cells. Such a histopathological pattern is frequently observed
357 in MSI tumors[37]. The MSI tumors have been linked to a favorable prognosis [38, 2], characterized with
358 lower differentiation grade, increased T-cell infiltration, and reduced susceptibility to invasiveness and
359 *KRAS* mutation [38], however, are commonly identified through separate MSI analysis and/or additional
360 immunohistochemical staining for mismatch repair enzymes in pathology diagnostics[3, 2, 38].

361 Furthermore, we also noted HPC 39 containing predominately healthy colon tissue associated with
362 better survival. The interpretation arises from the nature of the multivariable analysis where the 47
363 HPCs were modeled simultaneously. One can interpret this result as, while holding the other 46 HPCs
364 constant, patients with more abundance of healthy colon tissue showed an improved survival. The
365 higher proportion of healthy colon tissue may indicate relatively smaller or less aggressive tumors.
366 Indeed, within routine TNM assessments, lower pathological T-stage is known to lead to an improved
367 survival[3].

368 In the GSEA analysis, we noted a remarkable concurrence in AVANT-experimental group between
369 clustering based on cancer hallmark pathways and outcome-related HPCs, while such alignment was
370 much less pronounced in the standard-of-care group. One possible explanation is the heterogeneity of
371 patients in the TCGA-COAD dataset. In contrast to the well-defined treatment protocol in AVANT,
372 TCGA-COAD patients encompass diverse disease and demographic profiles. Consequently, this diversity
373 led to a wide spectrum of treatments, including surgical, neoadjuvant, and adjuvant therapies. The
374 survival-related HPCs discovered in the TCGA-COAD could therefore be, if related at all, to multiple
375 distinctive biological pathways. A general alignment observed in the AVANT-experimental group was
376 therefore not anticipated in the standard-of-care group.

377 In the AVANT-experimental group however, several survival-favoring HPCs either directly correlated
378 with VEGFa expression or were associated to enrichment in oncogenic pathways involving VEGFa gene,
379 indicating a favorable responses to the contentious bevacizumab treatment. In particular, HPC 5,
380 primarily characterized by necrosis, emerged as a significant contributor to enhanced survival, displaying
381 a positive correlation with VEGFa expression, which is the target of bevacizumab. Necrosis promotes

382 the expression of VEGFa, as dying tumor cells release signals that stimulate the growth of new blood
383 vessels [26]. In addition, survival-favoring HPCs 18, 27, and 31 were associated with enriched hypoxia
384 and angiogenesis pathways which also involve the VEGFa gene. We hypothesize that patients exhibiting
385 a higher abundance of HPC 5, 18, 27, and 31 may correspondingly express elevated levels of VEGFa,
386 the target of bevacizumab, which in turn result in a more favorable response to this treatment.

387 Oxaliplatin plus 5-fluorouracil-based regimens of XELOX and FOLFOX-4 are standard chemother-
388 apy for colorectal cancer[39]. Nonetheless, the treatment response is still modest with an estimate
389 rate of approximately 50% [1, 39], and the prediction of which patients will respond to this adjuvant
390 chemotherapy remains challenging. We observed enrichment in oncogenic pathways that may be within
391 the context of XELOX and FOLFOX-4 treatments in the AVANT trial. Survival-unfavorable HPCs
392 (12, 38, 14, 24, 20) were linked to the *KRAS* signaling-up pathway. In line with previous literature,
393 several *KRAS* mutations activate downstream signaling pathways and the *KRAS G12D* mutation was
394 predictive of an inferior response to FOLFOX [40]. Interestingly, HPCs 12, 14, and 38 contained muti-
395 nous tumors tissue, which has also been linked to *KRAS* mutational burden [37, 41]. Survival-favoring
396 HPCs (5, 31, 34, 26, 18, 27) were associated with enrichment in pathways of cell cycle, signalling,
397 DNA repair, and growth (i.e. G2/M checkpoint, E2F targets, Myc targets, and mTORC1 signaling),
398 while survival-unfavorable HPCs (12, 41, 38, 14, 24, 40, 20) linked to a depletion of those pathways.
399 Interestingly, patients with altered DNA repair capacity showed greater benefits from treatment with
400 oxaliplatin[39]. Moreover, carriers of MNAT1 gene, which is one of the leading genes in the G2/M check-
401 point pathway[42], were linked to better treatment outcome of FOLFOX[39]. A plausible mechanism
402 is that patients exhibiting activated oncogenic activities within these pathways might harbor a greater
403 abundance of targets suitable for oxaliplatin-based cytotoxic chemotherapy.

404 Another finding was our HPC-based prediction on OS outperforming the clinical baseline model.
405 This HPC-based risk classifier remained an independent prognostic factor (HR 2.50, 95% CI 1.18-
406 5.31) after adjusting for crucial clinical and demographic variables including TSR and tumor stage.
407 This finding aligns with recent findings reported by Jiang et al. [11]. Interestingly, although both
408 HPCs and TSR were derived from H&E slides, they appeared to encapsulate distinct non-overlapping
409 information. A potential explanation could be that the HPC-based classifier captures intricate details,
410 while TSR assessment requires a broader contextual understanding, not fully attainable with small image
411 patches [31]. Comparing our OS prediction directly with previous studies poses further challenges due

412 to differences in cancer types (e.g., colorectal [10, 43, 11] instead of colon cancer only), varied outcomes
413 (e.g., 5-year disease-free survival [DFS] [10]), diverse statistical measures (e.g., hazard ratio [43]), and
414 absence of independent test sets[12] in prior studies. Nevertheless, a recently study reported a test
415 set c-index of 0.65 for OS prediction in colorectal cancer[11] aligning with our reported c-index in the
416 context of colon cancer.

417 Building upon the aforementioned findings, this study showcases the prospective clinical utility of
418 AI-generated HPCs (Figure 7). Cancer WSIs were preprocessed into image patches and subsequently
419 used to train SSL encoders and to form HPCs. These HPCs serve as condensed representations of the
420 original WSIs, ready to be inspected by pathologists and enabling flexible linkage to molecular data.
421 These HPCs hold promise in classifying tumor characteristics, potentially predicting patient prognosis
422 and discerning distinct sensitivity groups to various therapies. In turn, this prediction can aid decision-
423 making in future multidisciplinary meetings. Moreover, this algorithm operates in a self-supervised
424 manner, affording enhanced transferability among datasets, flexible linkage to multimodal omics data,
425 and broader applicability across various outcome domains.

426 Despite the interesting findings, the study also has several limitations. The identification of HPCs
427 was based on small image tiles as is imperial to model training, while information regarding the larger
428 context is likely lost, as also stated above. For example, it is often challenging to distinguish aligned and
429 organized tumor stromal 'strands' from muscle tissue through traditional microscopic assessment [44].
430 Therefore, pathologists typically make this distinction based on contextual cues, color variances, or use
431 additional immunohistochemical stainings, all of which is not available within the small image patches.
432 Another limitation pertains to using TCGA as the training set. Although the TCGA is a large open
433 sourced database, it depends on the availability of registered clinicopathological data. This introduces
434 potential bias and variability in data quality across participating institutions. Moreover, due to data
435 availability, we were only able to focus on predicting OS rather than DFS which may better reflect tumor
436 behavior and biology[22, 45]. Lastly, due to the AVANT treatment regimen design, separate analysis
437 regarding bevacizumab or oxaliplatin-based chemotherapy was not attainable. Nonetheless, we made
438 efforts to differentiate between their distinct mechanisms by conducting histopathological inspections
439 and correlating the findings with immune landscape and oncogenic pathways.

440 In conclusion, our study employed a self-supervised approach to identify and validate histopatho-
441 logical features in colon cancer that are recognizable by human eyes and relevant to prognosis. These

442 features were interpreted through a pathology-focused perspective. Our results highlighted the clinical
443 significance of tumor tissue type, stromal amount and architecture, and the involvement of immune
444 cells. Integration of histopathological features with genetic and gene expression data unveiled potential
445 insights into oncogenic pathways and their relation to patient survival. Utilizing data from the clinical
446 AVANT trial, we proposed mechanisms influencing patient sensitivity to diverse treatments. Future re-
447 search should focus on refining prediction accuracy and validating the proposed mechanisms regarding
448 the therapeutic strategies in colon cancer.

449 **Methods**

450 **Study population**

451 The TCGA-COAD dataset was used for training and extracting features and histologic patterns using
452 SSL. This dataset consisted of 451 WSIs from 444 unique patients[22] with matched genetic and tran-
453 scriptomic information. We excluded duplications and WSIs with erroneous resolution that were not
454 suitable for the analyses (i.e. only several kilobytes in size). The final TCGA training set included 435
455 WSIs from 428 patients with a diagnosed pathological TNM-stage I-IV colon carcinoma (333 alive, 94
456 dead, and 1 missing vital status). We referred to the source population which TCGA-COAD represent-
457 ing as the "standard-of-care" group, contrasting it with the clinical trial data described below.

458 As external dataset we leveraged a study comprising 1213 colon cancer patients with available di-
459 agnostic H&E WSIs (one WSI per patient) as part of the clinical Bevacizumab-Avastin® adjuVANT
460 (AVANT) trial[23, 24]. Bevacizumab, a humanized anti-vascular endothelial growth factor (VEGF) mon-
461 oclonal antibody, had initially been shown to improve the OS in patients with metastatic colon cancer
462 when jointly used with the standard chemotherapy[26]. In the phase III AVANT trial, with an intent-to-
463 treat population of 3451 patients, an open-label design was used[23]. Patients were randomly assigned
464 in a 1:1:1 ratio to three different treatment regimens: FOLFOX-4 (intravenous 5-fluorouracil/folinic
465 acid plus oxaliplatin), bevacizumab-FOLFOX-4, and bevacizumab-XELOX (oral capecitabine plus in-
466 travenous oxaliplatin)[23]. The study aimed to investigate whether adding bevacizumab to the standard
467 oxaliplatin-based adjuvant chemotherapy could improve DFS among patients with stage II-high risk and
468 III colon cancer[23]. However, the trial was prematurely terminated due to the serious adverse effect

469 on the patient's OS in the bevacizumab-treated group[23]. The AVANT trial was chosen also due to
470 the previously studied potential correlation of VEGF, the stromal compartment (e.g. the TSR), and
471 patient prognosis[24, 32, 31]. For a detailed overview of the trial and patient characteristics, see Zunder
472 et al[24].

473 Given the unique treatment regimen of bevacizumab and its adverse effect in non-metastatic colon
474 cancer, as also proven by a predecesing clinical trial, the NSABP protocol C-08 trial [46], we decided
475 to primarily validate OS prediction, trained in the TCGA-COAD, within the control group who only
476 received FOLFOX-4 (without bevacizumab) and refer to it as the "AVANT control group". Subse-
477 quently, as several phase III trials had demonstrated that FOLFOX and XELOX are comparable in the
478 context of metastatic colorectal cancer[26, 27, 28], we thus combined the bevacizumab+FOLFOX-4 and
479 bevacizumab+XELOX groups into a unified "AVANT-experimental group" and conducted a separate
480 analysis to predict OS within the bevacizumab-treated patients.

481 The present study was performed by using anonymized archival material, not necessitating new
482 informed consent. Archival material was derived from the AVANT-trial (BO17920), performed in accor-
483 dance with the declaration of Helsinki[23, 24]. Protocol approval was obtained from the local medical
484 ethics review committees or institutional review boards at participating sites.

485 **Data pre-processing**

486 **Tissue segmentation and image tiling**

487 We used the preprocessing methods described in our previous study[47]. Tissue areas in WSIs were
488 segmented against background at 10x magnification level (pixel size approximate 1.0 um). WSIs were
489 divided into non-overlapping image tiles of size 224x224 pixels. The selection of a 10x magnification was
490 based on two key considerations. Firstly, it aligns with the standard magnification utilized by pathol-
491 ogists during microscopic assessments in clinical practice. Secondly, we conducted visual inspections of
492 tiles at 20x, 10x, and 5x magnifications, and found that tiles at 10x magnification provided an optimal
493 balance of capturing sufficient detail while also offering a reasonably sized overview of the morpholog-
494 ical structure. In addition, to overcome the variability of color stains from different scan facilities in
495 the TCGA and AVANT cohorts, we further applied the color normalization[48]. In total, we obtained
496 1,117,796 tiles in the TCGA training set (i.e. TCGA-COAD), and 4,827,055 tiles in the AVANT external

497 test set (AVANT-COAD, consisting of the standard and experimental treatment groups).

498 **Extracting image features using Barlow Twins**

499 We trained the SSL Barlow Twins feature extractor based on 250,000 image tiles randomly selected
500 from the TCGA-COAD dataset. The Barlow Twins extracted unique latent vectors (128 dimension)
501 from the preprocessed image tiles in TCGA. The model is based on ResNet-like architecture consisted
502 of several ResNet layers and one self-attention layer[17]. In essence, the Barlow Twins calculates the
503 cross-correlation matrix between the embedding outputs of two identical twin networks, both fed with
504 distorted versions of the same image tile[18]. It is optimized to make the correlation matrix close to the
505 identity matrix[18]. We used the batch size of 64 trained on a single NVIDIA® Tesla V100 GPU for
506 60 epochs. The Barlow Twins feature extractor was frozen after the training and used to project image
507 tiles into latent representation in the entire TCGA training set.

508 To facilitate the downstream analysis, we also applied five-fold CV partition in the TCGA-COAD
509 training set on patient level balanced the on American Joint Committee on Cancer (AJCC) TNM stage,
510 survival outcomes (i.e. death or censor), and binned survival time categories.

511 **Leiden community detection algorithm**

512 The Leiden clustering algorithm is a graph-based clustering algorithm that aims to identify distinct
513 communities or clusters within graph data [49]. In brief, it optimizes the modularity function (Equa-
514 tion 1), in such way to maximize the difference between the actual number of edges and the expected
515 number of edges in a community[49]. This modularity function also includes a resolution parameter γ ,
516 with higher values leading to more clusters and lower values leading to fewer clusters. Leiden clustering
517 is initiated by assigning each node in the graph to its own individual cluster, treating them as separate
518 communities, then iteratively optimizes the modularity function by moving a node from its current cluster
519 to a neighboring cluster or by merging clusters until the algorithm converged and revealing distinct
520 communities or clusters. We employed the Leiden clustering in a particular workflow. We began by
521 constructing a neighborhood graph using the $K=250$ nearest neighbors from a pool of 200,000 randomly
522 selected latent image vectors from a training set. Subsequently, we applied the Leiden algorithm to
523 identify clusters within this neighborhood graph. These cluster labels were then propagated to each

524 individual image tile across the entire dataset, once more utilizing the K-nearest neighbors approach.

$$\mathcal{H} = \frac{1}{2m} \sum_c \left(e_c - \gamma \frac{K_c^2}{2m} \right) \quad (1)$$

525 Modularity measures the difference between the actual number of edges in a community and the expected number of such edges. e_c denotes the actual number of edges in community c and the expected number of edges is expressed as $\frac{K_c^2}{2m}$, where K_c is the sum of the edges of the nodes in community c and m is the total number of edges in the network. γ is the resolution parameter, with higher values leading to more clusters and lower values leads to fewer clusters.

526 Identification of Histomorphological Phenotype Clusters (HPCs)

527 We identified HPCs as clusters obtained from the Leiden community detection algorithm operated on
528 128-dimensional image features extracted through the Barlow Twins encoder. The Leiden method was
529 also used for quality control to eliminate artifacts and underfocused image tiles. Quality control was
530 carried out after training the Barlow Twins and extracting image features. In the overall process, we
531 initially generated a substantial number of Leiden clusters. Next, we visually examined sample image
532 tiles from each cluster and removed clusters exhibiting artifacts such as air bubbles, foreign objects, etc.,
533 or those containing under-focused images. In particular, within the training set of a randomly selected
534 CV fold (fold 0), we randomly selected 200,000 latent image vectors to generate Leiden clusters. We
535 obtained 125 clusters at a high resolution of $\gamma = 6$. The Leiden labels were propagated into the entire
536 TCGA set using again the KNN methods. Next, we inspected randomly selected sample tiles ($N=32$)
537 from each cluster and identified 12 clusters containing predominately artifacts or underfocused images.
538 Image tiles labelled by these 12 clusters were subsequently removed from the further analyses. The HPCs
539 were newly derived in this cleaned dataset by re-running the Leiden clustering. Optimization of the
540 HPCs was conducted using primarily unsupervised methods and secondarily confirmed using supervised
541 methods. Importantly, both the two approaches converged on the same optimal Leiden resolution, as
542 elaborated below.

543 **Optimization of HPCs using unsupervised methods**

544 Leiden resolutions (i.e. $\gamma = 0.4, 0.7, 1.0, 1.5, 2.5,$ and 3.0) were optimized using three unsupervised
545 statistical tests: the Disruption score, Silhouette score, and Daves-Boundin index. Due to the potentially
546 high variance in data from the different institutions in the TCGA, all three scores were weighted by
547 the mean percentage of the institution presence in each cluster. We consistently identified the optimal
548 Leiden resolution as 1.5 through the three aforementioned statistical tests (Supplementary Figure 1a).

549 **Optimization of HPCs and the prediction of overall survival (OS) using Cox regressions** 550 **with L2 regularization**

551 To identify optimal HPC configurations and their associations with patient OS, we trained L2 regularized
552 Cox regressions for OS prediction using 5-fold CV. The Cox regressions were trained separately among
553 standard-of-care colon cancer patients (i.e. TCGA-COAD) and among the AVANT-experimental group.
554 *OS prediction in the standard-of-care group* Prediction of OS from HPCs among the standard-of-care
555 group was trained within TCGA-COAD using 5-fold CV and tested in the independent AVANT control
556 group. Specifically, for each CV fold within TCGA-COAD, we began by generating a range of Leiden
557 clustering configurations at various resolutions, including gamma values of 0.4, 0.7, 1.0, 1.5, 2.5, and 3.0,
558 using the method described earlier. Next, at each Leiden resolution, we calculated the compositional
559 representation of HPCs for each WSI (see Main Figure 1c), followed by a center-log-ratio transformation
560 (Equation 2). This transformation was designed to mitigate inter-dependencies among HPCs, ensuring
561 that the independence assumptions required for subsequent Cox regression analysis were met. The L2
562 regularized Cox regressions were then trained at the patient level, with one WSI per patient considered.
563 At each Leiden resolution, we performed a multivariable L2 regularized Cox regression, incorporating
564 all center-log-ratio-transformed HPCs specific to that resolution. We fine-tuned L2 regularizer (alpha)
565 through an iterative process involving 50 steps, spanning the alpha range from 10^{-4} to 10^4 . This
566 sequence of steps was repeated across all five cross-validation folds. The optimal Leiden resolution and
567 L2 regularizer was selected based the CV C-index.

568 Through this optimization process, the optimal Leiden resolution was determined to be 1.5, and the
569 L2 regularizer alpha was fixed at 0.1842. Of the note, this optimal Leiden resolution of 1.5 concurred with
570 the result from the unsupervised approaches. An HPC-based classifier was determined by the median

571 predicted hazard obtained in the TCGA-COAD. Once the Cox model is optimized, we evaluated the
572 final model performance in the external test set consisting of the AVANT-standard care group. First, the
573 47 HPCs were integrated into the AVANT-standard care group by employing the K-nearest neighbors
574 method (K=250), where each AVANT tile's HPC label was determined based on the majority votes
575 from its nearest neighbors in the TCGA training set. Next, the trained Cox model, with optimized
576 regularization and parameter estimates for the HPCs, was then applied to the AVANT-standard care
577 group to test the prediction of OS (Supplementary Figure 2b).

578 Furthermore, employing the same CV method, we trained a clinical baseline model on OS in TCGA-
579 COAD using L2 regularized Cox regression incorporating age, sex, TNM staging, and TSR as predictors.
580 We observed a c-index of 0.58 (bootstrap 95% CI 0.49-0.67) in the independent AVANT AVANT-
581 standard care group and the model-based risk classifier did not reach the statistical significance level
582 (Supplementary Figure 2c). This baseline model illustrates a simulation of decision-making in clinical
583 practice as control, using the most readily available and relevant clinical and demographic variables.
584 Our HPC-based model outperformed this clinical baseline model. In addition, we explored whether
585 the HPC-based classifier add additional prognostic value to the existing important clinical predictors.
586 We fitted an ordinary multivariable Cox regression within the external AVANT-standard care group,
587 including HPC-based classifier, sex, age, tumor-stroma ratio, and AJCC stage (Supplementary Figure
588 2d).

$$\text{clr}(x_i) = \ln\left(\frac{x_i}{g}\right), x_i = \frac{\text{counting of tiles in } C_i}{\text{total number of tiles in each WSI}}, g = \left(\prod_{i=1}^n x_i\right)^{\frac{1}{n}} \quad (2)$$

The center-log-ratio transformation (clr) calculates the natural logarithm of the
ratio (x_i) of compositional data for a specific cluster (C_i) to the geometric
(g) of the compositional data across all clusters. The compositional data (x_i) is
589 obtained by dividing the counting of tiles in cluster C_i by the total number of tiles
in each WSI. The geometric mean (g) is computed by multiplying the compositional
data values (x_i) for each cluster (C_i), ranging from $i = 1$ to n (where n is the total
number of clusters), and raising the resulting product to the power of $\frac{1}{n}$.

590 *OS prediction in the AVANT-experimental group*

591 Bevacizumab, a unique intervention investigated in the AVANT trial, was unlikely accessed by
592 patients from the TCGA-COAD cohort. Considering the significant poor prognostic outcome associated

593 with bevacizumab in non-metastatic colorectal cancer, we postulated that the relationship between
594 HPCs on OS might be influenced by this intervention. Furthermore, we hypothesized that estimates of
595 HPCs on OS trained from the general COAD population, such as TCGA, might not be applicable to
596 bevacizumab-treated patients.

597 To address these hypotheses, we conducted a separate 5-fold CV estimating the relationship between
598 HPCs and OS within the bevacizumab-treated patients (AVANT-experimental group). Similarly, we
599 generated 5-fold train-validation split stratified by TNM stage and survival time. We used the same
600 sets of HPCs obtained at the previously optimized Leiden 1.5 resolution. Similarly, we modelled the
601 center-log-transformed compositional data of HPCs on OS using Cox regressions with L2 regularization.
602 We fine tuned the L2 regularizer specifically for AVANT-experimental group. The model performance
603 of HPCs on OS prediction was evaluated using c-index in the 5-fold CV validation sets.

604 To understand the importance of each HPC on OS, we employed SHAP values[50]. SHAP values
605 measure the marginal contribution of a HPC towards the predicted OS, considering all possible com-
606 binations of features. We highlighted top 20 important HPCs favoring and hindering survival for both
607 standard-of-care and AVANT-experimental treated COAD patients.

608 **Interpretation of HPCs**

609 **Plotting HPCs using UMAP and PAGA plot**

610 We applied UMAP dimensionality reduction [51] to TCGA-COAD tile vector representations (128-
611 dimensional vectors), color-coded by 47 HPC IDs using optimized Leiden clustering configuration from
612 the prior step. Next, we generated a PAGA plot where each HPC is a node connected by lines based on
613 vector similarity. Pie charts within each HPC node showed annotated tissue type percentages annotated
614 independently by three experts (ASLPC, JHJMvK, and MP) (see below). We analyzed this plot to
615 identify and describe significant interconnected clusters (see Main Figure 2b). Based on the PAGA
616 plot, we also defined the "super-clusters" according to the interconnections among HPCs and tissue
617 composition (see Main Figure 2b).

618 **Pathologist assessment of HPCs**

619 **Histopathological assessment and characterization of HPCs** The histomorphological features
620 of 47 HPCs derived in TCGA training set were comprehensively and independently analyzed by two
621 expert pathologists (ASLPC and JHJMvK) and one medical researcher (MP). The analysis was exclu-
622 sively conducted using image tiles and the assessors were kept blinded to results from other analyses.
623 Specifically, we randomly selected a set of 32 tiles from each HPC within TCGA and each individual
624 tile was examined with specific focus on tumor epithelium, tumor stroma, and immune cells. Attention
625 was also paid to general tumor differentiation grade, tumor stromal amount, stromal classification, i.e.
626 aligned or disorganized, stromal neovascularization or other notable patterns (e.g. dysplastic tissue,
627 fatty tissue, muscle tissue fibers, blood vessels, erythrocytes, etc.)[3, 32, 44]. Each assessor evaluated
628 the tissue composition based on 32 randomly selected tiles per HPC, providing an average tissue com-
629 position for each HPC. In cases of conflicting tissue annotations, the assessors carried out discussions to
630 achieve consensus. In addition, a short label was given to each HPC based on tissue annotation either
631 according to the first and second predominant tissue types and patterns (e.g. "aligned stroma - well
632 differentiated tumor epithelium"), or as the single most dominant tissue type covering $\geq 70\%$ area of an
633 average tile (e.g. "necrotic"). The tissue description, composition, and short labels of all 47 HPCs were
634 displayed in Supplementary Table 1.

635 **Assessment of HPC consistency within and across TCGA and AVANT cohorts** We per-
636 formed various qualitative and quantitative analyses to evaluate the within-cluster and between-cluster
637 heterogeneity of HPCs, as well as their transferability from TCGA to AVANT cohorts. Initially, quali-
638 tative visual assessments were independently conducted by three experts (ASLPC, JHJMvK, and MP)
639 to evaluate the concordance within and discordance between HPCs. This evaluation followed the estab-
640 lished protocol for tissue type analysis, utilizing the previously randomly selected 32 tiles per HPC. The
641 assessors noted consistent histomorphological patterns within HPCs and diverse patterns across various
642 HPCs.

643 In addition, we conducted quantitative objective tests within TCGA and AVANT tiles separately
644 to determine if the learned morphological features of the HPCs could be replicated by human eyes. We
645 displayed three rows, each containing five tiles, which is referred to as a "question". Among these rows,
646 two belonged to the same HPC, while the third row, also referred to as the "odd HPC", were tiles

647 randomly selected from a different HPC. All example tiles were randomly selected within each HPC.
648 The researcher (MP) was required to identify the "odd HPC", and upon doing so, the next question
649 was presented (example shown in Supplementary Figure 2). In order to calculate the success rate, we
650 ran 50 questions per HPC and we repeated the experiment for all 47 HPCs. The test was conducted
651 on a closed website accessible through login and was conducted separately for tiles randomly selected
652 from TCGA and AVANT. The conducted experiment exhibited an average completion time of under
653 10 seconds per question. The success rate was determined for each HPC by dividing the number of
654 incorrect answers by the total number of questions (50 questions per HPC). We hypothesized that most
655 HPCs would be distinguishable. However, some HPCs may be challenging to differentiate due to tissue
656 similarities, either within the same super-cluster or through similar tissue morphology (e.g., muscle
657 tissue and tumor stroma). The results showed that HPCs in close proximity to each other in the PAGA
658 or belonging to the same super-cluster were indeed more prone to being mistaken.

659 To validate HPCs derived from the TCGA training set were generalized well in the external AVANT
660 test set, three assessors independently carried out visual examination of tissue characteristics in 32
661 randomly selected tiles from each HPC in both the AVANT trial and the TCGA set, comparing their
662 histomorphological features regarding tissue types and composition established in the previous step.
663 Assessors confirmed that the consistent and meaningful patterns learned by the Barlow Twins, could be
664 replicated across other clinical cohorts like the AVANT trial. To validate our observation, we compared
665 the objective test results between TCGA and AVANT, focusing on the overlap in both misclassified and
666 correctly classified HPCs across the datasets.

667 **Linkage between survival-related HPCs, immune landscape, and gene expression data**

668 We calculated Spearman correlations between HPCs and RNASeq-derived immune features from TCGA-
669 COAD data, correcting for false discovery rate (0.05) using Benjamini-Hochberg correction. We cre-
670 ated bi-hierarchical clusters for immune features and top 20 significant HPCs linked to OS in both
671 standard-of-care and AVANT-experimental groups. Clustering was based on correlation coefficients
672 using Euclidean distance and Ward's aggregation.

673 In addition, we performed GSEA to explore the potential associations between HPCs and the major
674 cancer hallmark pathways, as previously described [52]. The analysis was conducted within 282 TCGA-
675 COAD patients with available gene expression data for 20,530 genes. For each HPC, we calculated the

676 Spearman correlation coefficients with the expression data of these 20,530 genes and sorted the resulting
677 correlation coefficients to rank the genes in a descending order. Subsequently, enrichment scores for 50
678 major cancer hallmark pathways, as defined by the "MSigDB_Hallmark_2020" gene set [42], were
679 computed for each HPC based on the generated ranked gene list. A positive enrichment score indicated
680 higher composition of a HPC was associated with gene enrichment in a pathway and a negative value
681 suggested higher composition of a HPC was associated with underrepresentation of a pathway. We
682 plotted the cancer hallmark enrichment scores for the top 20 important HPCs related to OS, for both
683 the general and experimental treatment groups. We set a significance level of 0.01 of the false discovery
684 q value. The analysis was conducted using the gseapy (1.0.4) Python package. Two-way hierarchical
685 clustering was based on the Euclidean distance of the enrichment scores and Ward's aggregation method.

686 Code and data availability

687 All data analyses are based upon publicly available Python software packages and codes are avail-
688 able from our previous publication ([https://github.com/AdalbertoCq/Histomorphological-Phenotype-
689 Learning](https://github.com/AdalbertoCq/Histomorphological-Phenotype-Learning))[17]. The data that support the findings of this study are available from Genentech Inc., Roche
690 but restrictions apply to the availability of these data, which were used under licence for the current
691 study, and so are not publicly available. Data are however available from the authors upon reasonable
692 request and with permission of Genentech Inc., Roche.

693 Acknowledgements

694 The work is supported by the Swedish Research Council (BL, 2019-06360), NCI/NIH Cancer Center
695 Support Grant (AT, P30CA016087), and the Bollenstreekfonds, Lisse, Netherlands (WEM). We thank
696 the team of NYU Langone High Performance Computing (HPC) Core's resources supporting us to per-
697 form the analysis. We would like to thank the NYU Applied Bioinformatics Laboratories (ABL) for
698 providing bioinformatics support and helping with analysis of the data. ABL is a shared resource par-
699 tially supported by the Cancer Center Support Grant P30CA016087 at the Laura and Isaac Perlmutter
700 Cancer Center. We would also like to thank Leslie Solorzano for her input in data preprocessing. The
701 AVANT-trial (BO17920) was originally financed by Genentech Inc., Roche, Switzerland. The authors
702 thank Nikolas Jan Rakebrandt as liaison from Roche.

703 **Author contributions**

704 B.L. executed data processing, model training, and data analyses. A.C.Q., N.C., and B.L. wrote python
705 codes used to run all the experiments. M.P. and W.E.M. provided coordination in obtaining H&E slides
706 and corresponding data from Bevacizumab-Avastin® adjuVANT trial. M.P., A.S.L.P.C, J.H.J.M.v.K,
707 provided histological assessment and interpretation of HPCs. B.L. and M.P. wrote the first draft of
708 the manuscript which was later revised and approved by all co-authors. B.L., N.C., A.C.Q, T.S., A.T.
709 provided expertise in deep learning, biostatistics, and bioinformatics. M.P., A.S.L.P.C, J.H.J.M.v.K,
710 R.A.E.M.T, and W.E.M provided expertise in colon cancer histopathology and biology. A.T. supervised
711 the study.

712 **Declaration of interests**

713 AT is a co-founder of Imagenomix. The remaining authors declare no competing interests.

714 References

- 715 [1] James D Brierley, Mary K Gospodarowicz, and Christian Wittekind. *TNM classification of malig-*
716 *nant tumours*. John Wiley & Sons, 2017.
- 717 [2] G. Argilés, J. Tabernero, R. Labianca, D. Hochhauser, R. Salazar, T. Iveson, P. Laurent-Puig,
718 P. Quirke, T. Yoshino, J. Taieb, E. Martinelli, and D. Arnold. Localised colon cancer: Esmo clinical
719 practice guidelines for diagnosis, treatment and follow-up†. *Annals of Oncology*, 31(10):1291–1305,
720 2020.
- 721 [3] Martin R Weiser. Ajcc 8th edition: colorectal cancer. *Annals of surgical oncology*, 25:1454–1455,
722 2018.
- 723 [4] A Cervantes, R Adam, S Roselló, D Arnold, N Normanno, J Taïeb, J Seligmann, T De Baere,
724 P Osterlund, T Yoshino, et al. Metastatic colorectal cancer: Esmo clinical practice guideline for
725 diagnosis, treatment and follow-up. *Annals of Oncology*, 34(1):10–32, 2023.
- 726 [5] Eileen Morgan, Melina Arnold, A Gini, V Lorenzoni, CJ Cabasag, Mathieu Laversanne, Jerome
727 Vignat, Jacques Ferlay, Neil Murphy, and Freddie Bray. Global burden of colorectal cancer in 2020
728 and 2040: Incidence and mortality estimates from globocan. *Gut*, 72(2):338–344, 2023.
- 729 [6] Aoife Maguire and Kieran Sheahan. Controversies in the pathological assessment of colorectal
730 cancer. *World journal of gastroenterology: WJG*, 20(29):9850, 2014.
- 731 [7] Kaustav Bera, Kurt A Schalper, David L Rimm, Vamsidhar Velcheti, and Anant Madabhushi.
732 Artificial intelligence in digital pathology—new tools for diagnosis and precision oncology. *Nature*
733 *reviews Clinical oncology*, 16(11):703–715, 2019.
- 734 [8] Mohsin Bilal, Shan E Ahmed Raza, Ayesha Azam, Simon Graham, Mohammad Ilyas, Ian A Cree,
735 David Snead, Fayyaz Minhas, and Nasir M Rajpoot. Development and validation of a weakly
736 supervised deep learning framework to predict the status of molecular pathways and key mutations
737 in colorectal cancer from routine histology images: a retrospective study. *The Lancet Digital Health*,
738 3(12):e763–e772, 2021.

- 739 [9] Veenu Rani, Syed Tufael Nabi, Munish Kumar, Ajay Mittal, and Krishan Kumar. Self-supervised
740 learning: A succinct review. *Archives of Computational Methods in Engineering*, pages 1–15, 2023.
- 741 [10] Ellery Wulczyn, David F Steiner, Melissa Moran, Markus Plass, Robert Reihs, Fraser Tan, Isabelle
742 Flament-Auvigne, Trissia Brown, Peter Regitnig, Po-Hsuan Cameron Chen, et al. Interpretable
743 survival prediction for colorectal cancer using deep learning. *NPJ digital medicine*, 4(1):71, 2021.
- 744 [11] Xiaofeng Jiang, Michael Hoffmeister, Hermann Brenner, Hannah Sophie Muti, Tanwei Yuan, Se-
745 bastian Foersch, Nicholas P West, Alexander Brobeil, Jitendra Jonnagaddala, Nicholas Hawkins,
746 et al. End-to-end prognostication in colorectal cancer by deep learning: a retrospective, multicentre
747 study. *The Lancet Digital Health*, 6(1):e33–e43, 2024.
- 748 [12] Richard J Chen, Ming Y Lu, Drew FK Williamson, Tiffany Y Chen, Jana Lipkova, Zahra Noor,
749 Muhammad Shaban, Maha Shady, Mane Williams, Bumjin Joo, et al. Pan-cancer integrative
750 histology-genomic analysis via multimodal deep learning. *Cancer Cell*, 40(8):865–878, 2022.
- 751 [13] Nicolas Coudray and Aristotelis Tsirigos. Deep learning links histology, molecular signatures and
752 prognosis in cancer. *Nature Cancer*, 1(8):755–757, 2020.
- 753 [14] Mingu Kang, Heon Song, Seonwook Park, Donggeun Yoo, and Sérgio Pereira. Benchmarking self-
754 supervised learning on diverse pathology datasets. In *Proceedings of the IEEE/CVF Conference*
755 *on Computer Vision and Pattern Recognition*, pages 3344–3354, 2023.
- 756 [15] Richard J Chen and Rahul G Krishnan. Self-supervised vision transformers learn visual concepts
757 in histopathology. *arXiv preprint arXiv:2203.00585*, 2022.
- 758 [16] Sophia J Wagner, Daniel Reisenbüchler, Nicholas P West, Jan Moritz Niehues, Jiefu Zhu, Sebastian
759 Foersch, Gregory Patrick Veldhuizen, Philip Quirke, Heike I Grabsch, Piet A van den Brandt, et al.
760 Transformer-based biomarker prediction from colorectal cancer histology: A large-scale multicentric
761 study. *Cancer Cell*, 41(9):1650–1661, 2023.
- 762 [17] Adalberto Claudio Quiros, Nicolas Coudray, Anna Yeaton, Xinyu Yang, Bojing Liu, Hortense Le,
763 Luis Chiriboga, Afreen Karimkhan, Navneet Narula, David A. Moore, Christopher Y. Park, Harvey
764 Pass, Andre L. Moreira, John Le Quesne, Aristotelis Tsirigos, and Ke Yuan. Mapping the landscape

- 765 of histomorphological cancer phenotypes using self-supervised learning on unannotated pathology
766 slides, 2024. Accepted for publication.
- 767 [18] Jure Zbontar, Li Jing, Ishan Misra, Yann LeCun, and Stéphane Deny. Barlow twins: Self-supervised
768 learning via redundancy reduction. In *International Conference on Machine Learning*, pages 12310–
769 12320. PMLR, 2021.
- 770 [19] Maximilian Ilse, Jakub Tomczak, and Max Welling. Attention-based deep multiple instance learn-
771 ing. In Jennifer Dy and Andreas Krause, editors, *Proceedings of the 35th International Conference*
772 *on Machine Learning*, volume 80 of *Proceedings of Machine Learning Research*, pages 2127–2136.
773 PMLR, 10–15 Jul 2018.
- 774 [20] Chengkuan Chen, Ming Y Lu, Drew FK Williamson, Tiffany Y Chen, Andrew J Schaumberg, and
775 Faisal Mahmood. Fast and scalable search of whole-slide images via self-supervised deep learning.
776 *Nature Biomedical Engineering*, 6(12):1420–1434, 2022.
- 777 [21] Corentin Gueréndel, Phil Arnold, and Ben Torben-Nielsen. Creating small but meaningful repre-
778 sentations of digital pathology images. In Manfredo Atzori, Nikolay Burlutskiy, Francesco Ciompi,
779 Zhang Li, Fayyaz Minhas, Henning Müller, Tingying Peng, Nasir Rajpoot, Ben Torben-Nielsen,
780 Jeroen van der Laak, Mitko Veta, Yinyin Yuan, and Inti Zlobec, editors, *Proceedings of the MICCAI*
781 *Workshop on Computational Pathology*, volume 156 of *Proceedings of Machine Learning Research*,
782 pages 206–215. PMLR, 27 Sep 2021.
- 783 [22] The cancer genome atlas program (tcga). [https://www.cancer.gov/ccg/research/genome-](https://www.cancer.gov/ccg/research/genome-sequencing/tcga)
784 [sequencing/tcga](https://www.cancer.gov/ccg/research/genome-sequencing/tcga). Accessed: 2023-05-09.
- 785 [23] Aimery de Gramont, Eric Van Cutsem, Hans-Joachim Schmoll, Josep Tabernero, Stephen Clarke,
786 Malcolm J Moore, David Cunningham, Thomas H Cartwright, J Randolph Hecht, Fernando Rivera,
787 et al. Bevacizumab plus oxaliplatin-based chemotherapy as adjuvant treatment for colon cancer
788 (avant): a phase 3 randomised controlled trial. *The lancet oncology*, 13(12):1225–1233, 2012.
- 789 [24] Stéphanie M Zunder, Gabi W van Pelt, Hans J Gelderblom, Christoph Mancao, Hein Putter,
790 Rob A Tollenaar, and Wilma E Mesker. Predictive potential of tumour-stroma ratio on benefit

- 791 from adjuvant bevacizumab in high-risk stage ii and stage iii colon cancer. *British Journal of*
792 *Cancer*, 119(2):164–169, 2018.
- 793 [25] F Alexander Wolf, Fiona K Hamey, Mireya Plass, Jordi Solana, Joakim S Dahlin, Berthold
794 Göttgens, Nikolaus Rajewsky, Lukas Simon, and Fabian J Theis. Paga: graph abstraction recon-
795 ciles clustering with trajectory inference through a topology preserving map of single cells. *Genome*
796 *biology*, 20:1–9, 2019.
- 797 [26] Herbert Hurwitz, Louis Fehrenbacher, William Novotny, Thomas Cartwright, John Hainsworth,
798 William Heim, Jordan Berlin, Ari Baron, Susan Griffing, Eric Holmgren, et al. Bevacizumab plus
799 irinotecan, fluorouracil, and leucovorin for metastatic colorectal cancer. *New England journal of*
800 *medicine*, 350(23):2335–2342, 2004.
- 801 [27] Leonard B Saltz, Stephen Clarke, Eduardo Díaz-Rubio, Werner Scheithauer, Arie Figer, Ralph
802 Wong, Sheryl Koski, Mikhail Lichinitser, Tsai-Shen Yang, Fernando Rivera, et al. Bevacizumab
803 in combination with oxaliplatin-based chemotherapy as first-line therapy in metastatic colorectal
804 cancer: a randomized phase iii study. *Journal of clinical oncology*, 26(12):2013–2019, 2008.
- 805 [28] Fairouz F Kabbinavar, Julie Hambleton, Robert D Mass, Herbert I Hurwitz, Emily Bergsland,
806 and Somnath Sarkar. Combined analysis of efficacy: the addition of bevacizumab to fluo-
807 rouracil/leucovorin improves survival for patients with metastatic colorectal cancer. *Journal of*
808 *clinical oncology*, 23(16):3706–3712, 2005.
- 809 [29] Tessa P Sandberg, Maaïke PME Stuart, Jan Oosting, Rob AEM Tollenaar, Cornelis FM Sier, and
810 Wilma E Mesker. Increased expression of cancer-associated fibroblast markers at the invasive front
811 and its association with tumor-stroma ratio in colorectal cancer. *BMC cancer*, 19(1):1–9, 2019.
- 812 [30] Gabi W van Pelt, Tessa P Sandberg, Hans Morreau, Hans Gelderblom, J Han JM van Krieken,
813 Rob AEM Tollenaar, and Wilma E Mesker. The tumour–stroma ratio in colon cancer: the biological
814 role and its prognostic impact. *Histopathology*, 73(2):197–206, 2018.
- 815 [31] Wilma E Mesker, Jan Junggeburst, Karoly Szuhai, Pieter de Heer, Hans Morreau, Hans J Tanke,
816 and Rob AEM Tollenaar. The carcinoma–stromal ratio of colon carcinoma is an independent

- 817 factor for survival compared to lymph node status and tumor stage. *Analytical Cellular Pathology*,
818 29(5):387–398, 2007.
- 819 [32] Stéphanie Zunder, Priscilla Van der Wilk, Hans Gelderblom, Tim Dekker, Christoph Mancao, Anna
820 Kiialainen, Hein Putter, Rob Tollenaar, and Wilma Mesker. Stromal organization as predictive
821 biomarker for the treatment of colon cancer with adjuvant bevacizumab; a post-hoc analysis of the
822 avant trial. *Cellular Oncology*, 42:717–725, 2019.
- 823 [33] Hideki Ueno, Yukihide Kanemitsu, Shigeki Sekine, Megumi Ishiguro, Eisaku Ito, Yojiro Hashiguchi,
824 Fukuo Kondo, Hideyuki Shimazaki, Yoshiki Kajiwara, Koichi Okamoto, et al. A multicenter study
825 of the prognostic value of desmoplastic reaction categorization in stage ii colorectal cancer. *The
826 American journal of surgical pathology*, 43(8):1015–1022, 2019.
- 827 [34] Hideki Ueno, Yoshiki Kajiwara, Yoich Ajioka, Tamotsu Sugai, Shigeki Sekine, Megumi Ishiguro,
828 Atsuo Takashima, and Yukihide Kanemitsu. Histopathological atlas of desmoplastic reaction char-
829 acterization in colorectal cancer. *Japanese Journal of Clinical Oncology*, 51(6):1004–1012, 2021.
- 830 [35] Franck Pagès, Bernhard Mlecnik, Florence Marliot, Gabriela Bindea, Fang-Shu Ou, Carlo Bifulco,
831 Alessandro Lugli, Inti Zlobec, Tilman T Rau, Martin D Berger, et al. International validation of
832 the consensus immunoscore for the classification of colon cancer: a prognostic and accuracy study.
833 *The Lancet*, 391(10135):2128–2139, 2018.
- 834 [36] Alexander Bagaev, Nikita Kotlov, Krystle Nomie, Viktor Svekolkina, Azamat Gafurov, Olga Isaeva,
835 Nikita Osokin, Ivan Kozlov, Felix Frenkel, Olga Gancharova, et al. Conserved pan-cancer microen-
836 vironment subtypes predict response to immunotherapy. *Cancer cell*, 39(6):845–865, 2021.
- 837 [37] Jinru Shia, Nikolaus Schultz, Deborah Kuk, Efsevia Vakiani, Sumit Middha, Neil H Segal, Jaclyn F
838 Hechtman, Michael F Berger, Zsofia K Stadler, Martin R Weiser, et al. Morphological character-
839 ization of colorectal cancers in the cancer genome atlas reveals distinct morphology–molecular
840 associations: clinical and biological implications. *Modern pathology*, 30(4):599–609, 2017.
- 841 [38] C Richard Boland and Ajay Goel. Microsatellite instability in colorectal cancer. *Gastroenterology*,
842 138(6):2073–2087, 2010.

- 843 [39] Elisabeth J Kap, Petra Seibold, Swantje Richter, Dominique Scherer, Nina Habermann, Yesilda
844 Balavarca, Lina Jansen, Natalia Becker, Katrin Pfütze, O Popanda, et al. Genetic variants in dna
845 repair genes as potential predictive markers for oxaliplatin chemotherapy in colorectal cancer. *The*
846 *pharmacogenomics journal*, 15(6):505–512, 2015.
- 847 [40] Gongmin Zhu, Lijiao Pei, Hongwei Xia, Qiulin Tang, and Feng Bi. Role of oncogenic kras in the
848 prognosis, diagnosis and treatment of colorectal cancer. *Molecular cancer*, 20(1):1–17, 2021.
- 849 [41] Shih-Ching Chang, Pei-Ching Lin, Jen-Kou Lin, Chien-Hsing Lin, Shung-Haur Yang, Wen-Yi
850 Liang, Wei-Shone Chen, and Jeng-Kai Jiang. Mutation spectra of common cancer-associated genes
851 in different phenotypes of colorectal carcinoma without distant metastasis. *Annals of surgical*
852 *oncology*, 23:849–855, 2016.
- 853 [42] Arthur Liberzon, Chet Birger, Helga Thorvaldsdóttir, Mahmoud Ghandi, Jill P Mesirov, and Pablo
854 Tamayo. The molecular signatures database hallmark gene set collection. *Cell systems*, 1(6):417–
855 425, 2015.
- 856 [43] Jakob Nikolas Kather, Johannes Krisam, Pornpimol Charoentong, Tom Luedde, Esther Herpel,
857 Cleo-Aron Weis, Timo Gaiser, Alexander Marx, Nektarios A Valous, Dyke Ferber, et al. Predicting
858 survival from colorectal cancer histology slides using deep learning: A retrospective multicenter
859 study. *PLoS medicine*, 16(1):e1002730, 2019.
- 860 [44] Gabi W van Pelt, Sanne Kjær-Frifeldt, J Han JM van Krieken, Raed Al Dieri, Hans Morreau,
861 Rob AEM Tollenaar, Flemming B Sørensen, and Wilma E Mesker. Scoring the tumor-stroma ratio
862 in colon cancer: procedure and recommendations. *Virchows Archiv*, 473:405–412, 2018.
- 863 [45] Jianfang Liu, Tara Lichtenberg, Katherine A Hoadley, Laila M Poisson, Alexander J Lazar, An-
864 drew D Cherniack, Albert J Kovatich, Christopher C Benz, Douglas A Levine, Adrian V Lee,
865 et al. An integrated tcga pan-cancer clinical data resource to drive high-quality survival outcome
866 analytics. *Cell*, 173(2):400–416, 2018.
- 867 [46] Carmen J Allegra, Greg Yothers, Michael J O’Connell, Saima Sharif, Nicholas J Petrelli, Linda H
868 Colangelo, James N Atkins, Thomas E Seay, Louis Fehrenbacher, Richard M Goldberg, et al. Phase

- 869 iii trial assessing bevacizumab in stages ii and iii carcinoma of the colon: results of nsabp protocol
870 c-08. *Journal of Clinical Oncology*, 29(1):11, 2011.
- 871 [47] Nicolas Coudray, Paolo Santiago Ocampo, Theodore Sakellaropoulos, Navneet Narula, Matija
872 Snuderl, David Fenyö, Andre L. Moreira, Narges Razavian, and Aristotelis Tsirigos. Classifica-
873 tion and mutation prediction from non–small cell lung cancer histopathology images using deep
874 learning. *Nature Medicine*, 24, 2018.
- 875 [48] Erik Reinhard, Michael Ashikhmin, Bruce Gooch, and Peter Shirley. Color transfer between images.
876 *IEEE Computer Graphics and Applications*, 21, 2001.
- 877 [49] Vincent A Traag, Ludo Waltman, and Nees Jan Van Eck. From louvain to leiden: guaranteeing
878 well-connected communities. *Scientific reports*, 9(1):5233, 2019.
- 879 [50] Scott M Lundberg and Su-In Lee. A unified approach to interpreting model predictions. *Advances*
880 *in neural information processing systems*, 30, 2017.
- 881 [51] Leland McInnes, John Healy, Nathaniel Saul, and Lukas Großberger. UMAP: Uniform Manifold
882 Approximation and Projection. *Journal of Open Source Software*, 3(29), 2018.
- 883 [52] Aravind Subramanian, Pablo Tamayo, Vamsi K Mootha, Sayan Mukherjee, Benjamin L Ebert,
884 Michael A Gillette, Amanda Paulovich, Scott L Pomeroy, Todd R Golub, Eric S Lander, et al.
885 Gene set enrichment analysis: a knowledge-based approach for interpreting genome-wide expression
886 profiles. *Proceedings of the National Academy of Sciences*, 102(43):15545–15550, 2005.